Evaluating the Diurnal and Semidiurnal Cycle of Precipitation in CMIP6 Models Using Satellite- and Ground-Based Observations

SHUAIQI TANG,[a] PETER GLECKLER,[a] SHAOCHENG XIE,[a] JIWOO LEE,[a] MIN-SEOP AHN,[a] CURT COVEY,[a]
AND CHENGZHU ZHANG[a]

[a] *Lawrence Livermore National Laboratory, Livermore, California*

ABSTRACT: The diurnal and semidiurnal cycle of precipitation simulated from CMIP6 models during 1996–2005 are evaluated globally between 60°S and 60°N as well as at 10 selected locations representing three categories of diurnal cycle of precipitation: 1) afternoon precipitation over land, 2) early morning precipitation over ocean, and 3) nocturnal precipitation over land. Three satellite-based and two ground-based rainfall products are used to evaluate the climate models. Globally, the ensemble mean of CMIP6 models shows a diurnal phase of 3 to 4 h earlier over land and 1 to 2 h earlier over ocean when compared with the latest satellite products. These biases are in line with what were found in previous versions of climate models but reduced compared to the CMIP5 ensemble mean. Analysis at the selected locations complemented with in situ measurements further reinforces these results. Several CMIP6 models have shown a significant improvement in the diurnal cycle of precipitation compared to their CMIP5 counterparts, notably in delaying afternoon precipitation over land. This can be attributed to the use of more sophisticated convective parameterizations. Most models are still unable to capture the nocturnal peak associated with elevated convection and propagating mesoscale convective systems, with a few exceptions that allow convection to be initiated above the boundary layer to capture nocturnal elevated convection. We also quantify an encouraging consistency between the satellite- and ground-based precipitation measurements despite differing spatiotemporal resolutions and sampling periods, which provides confidence in using them to evaluate the diurnal and semidiurnal cycle of precipitation in climate models.

KEYWORDS: Climate models; Convective parameterization; Model errors; Model evaluation/performance; Climate variability; Diurnal effects

1. Introduction

Precipitation is among the most important variables in the climate system (e.g., Trenberth et al. 2003) and diurnal cycle is a dominant component of its temporal variability (Dai 2006; Dai et al. 2007). The diurnal cycle of precipitation is forced by the diurnal variation of solar insolation but modulated by ocean–land contrast (e.g., Mori et al. 2004; Sato et al. 2009; Worku et al. 2019), surface orography (e.g., Fitzjarrald et al. 2008; Houze 2014; Junquas et al. 2018; Liu et al. 2009; Sato 2013), and propagating weather systems (e.g., Burleyson et al. 2016; Carbone et al. 2002; Filho et al. 2015; Greco et al. 1990; Janowiak et al. 2005; Jiang et al. 2006; Lee et al. 2007b; Machado et al. 2004). The diurnal cycle of precipitation, as well as the closely related moist convection and cloudiness, greatly affects the radiative budget at the surface and regulates surface temperature (Dai et al. 1999b).

Global climate models (GCMs), including those used in phase 5 of the Coupled Model Intercomparison Project (CMIP5; Taylor et al. 2012), were found to have difficulties in accurately simulating the diurnal cycle of precipitation (e.g., Covey et al. 2016). There are two common model errors. One is that GCM precipitation diurnal cycle peaks earlier than observed. Over land, most models tend to start raining in the morning and reach maximum rainfall soon after noontime, while the observed precipitation typically peaks in late afternoon (Dai 2006; Guichard et al. 2004; Yang and Slingo 2001). Over ocean, where observed precipitation peaks in early morning, many GCMs also simulate precipitation maximum a few hours earlier, although the diurnal cycle is relatively weak (Dai 2006; Yang and Slingo 2001). The second common model error is the missing nocturnal precipitation peak from GCMs in some regions such as the central United States (Lee et al. 2007b), the Amazon region (Dai 2006), northeast Argentina (Giles et al. 2020), and the eastern periphery of the Tibetan Plateau (Zhou et al. 2008). These errors are thought to be primarily related to the unrealistically strong coupling between model convection and surface fluxes and the inability of model to capture elevated convection or propagating mesoscale convective systems (Dai 2006; Lee et al. 2007a,b; Liang et al. 2004; Wang et al. 2015; Xie et al. 2002, 2019; Zheng et al. 2019; Wang et al. 2020). It has been suggested that deficiencies in moist convective parameterization largely account for the failure of capturing diurnal cycle of precipitation in climate models (Betts and Jakob 2002; Dirmeyer et al. 2012; Lee et al. 2008; Rio et al. 2009). In a recent study, Xie et al. (2019) demonstrated that simulation of the diurnal cycle of precipitation in climate models could be substantially improved by relaxing the coupling of convection to the surface heating and allowing air parcels to launch above the boundary layer to capture nocturnal elevated convection.

With the availability of 3-hourly or hourly datasets, the semidiurnal (twice daily) Fourier harmonic has also been examined in recent studies. The semidiurnal variation is typically weaker than the diurnal (once daily) harmonic (e.g., Covey et al. 2016; Dai et al. 2007) but in some regions accounts for a similar or greater variance than the diurnal cycle. This is particular true over the oceans (Dai 2001) and in central China between the Yangtze and

Table 1. CMIP6 models used in this study. Models with CMIP5 counterparts are selected for further comparison (see text).

Models	Institute	CMIP5 counterpart	Horizontal grid size (lon × lat)	No. of vertical levels	References
ACCESS-CM2	Commonwealth Scientific and Industrial Research Organization (CSIRO) and Bureau of Meteorology (BoM), Australia	ACCESS1.0	192 × 144	85	Dix et al. (2019)
BCC_CSM2-MR	Beijing Climate Center, China	BCC_CSM1.1-M	320 × 160	46	Wu et al. (2019)
CNRM-CM6.1	Centre National de Recherches Météorologiques, France		256 × 128	91	Voldoire et al. (2019)
E3SM-1.0	U.S. Department of Energy		360 × 180	72	Golaz et al. (2019)
EC-Earth3	European Centre for Medium-Range Weather Forecasts (ECMWF)	EC-Earth	512 × 256	91	Massonnet et al. (2020)
FGOALS-g3	Institute of Atmospheric Physics, Chinese Academy of Sciences, China	FGOALS-g2	180 × 80	30	Li et al. (2020)
GFDL-CM4	NOAA Geophysical Fluid Dynamics Laboratory		144 × 90	33	Held et al. (2019)
IPSL-CM6A-LR	Institute Pierre-Simon Laplace, France	IPSL-CM5A-LR	144 × 143	79	Hourdin et al. (2020)
KACE-1.0-G	National Institute of Meteorological Sciences, Korea Meteorological Administration, South Korea		192 × 144	85	Byun et al. (2019)
MIROC6	University of Tokyo, Japan	MIROC5	256 × 128	81	Tatebe et al. (2019)
MPI-ESM1.2-HR	Max Planck Institute, Germany		384 × 192	47	Mauritsen et al. (2019)
MRI-ESM2.0	Meteorological Research Institute, Japan Meteorological Administration, Japan		320 × 160	80	Yukimoto et al. (2019)
NESM3	Nanjing University of Information Science and Technology, China		192 × 96	47	Cao et al. (2018)
SAM0-UNICON	Seoul National University, South Korea		288 × 192	30	Park et al. (2019)
TaiESM1	Research Center for Environmental Changes, Taiwan, China		288 × 192	30	Lee et al. (2020)

Yellow Rivers (Zhou et al. 2008). However, most datasets used in previous studies are at 3-hourly temporal resolution. With only four time points per semidiurnal cycle, the sampling frequency is close to the Nyquist limit to resolve a sine wave (Nyquist 1928; Shannon 1949). Therefore, large uncertainties may exist in the previous semidiurnal cycle analysis.

The latest phase (phase 6) of CMIP (CMIP6; Eyring et al. 2016), archived by the Earth System Grid Federation (ESGF; Williams et al. 2016), includes the world's most recent climate models. In this study, we will evaluate the diurnal and semidiurnal cycles of precipitation simulated in CMIP6 models and compare their performances with the earlier version of CMIP5 models. We will use multiple state-of-the-art satellite-based high-resolution precipitation products and long-term ground-based precipitation measurements from the U.S. Department of Energy's (DOE's) Atmospheric Radiation Measurements (ARM) program to evaluate these models. Because the robustness of our model evaluation depends on the quality of these observational products, the strengths, weaknesses, and level of consistency of the satellite- and ground-based observations of precipitation are extensively discussed in this paper and demonstrated in our analysis.

The paper is organized as follows: Section 2 introduces the CMIP models and observational data used in this study. Section 3 shows the results of diurnal and semidiurnal cycles of precipitation globally between 60°S and 60°N as well as at 10 selected locations. Section 4 further discusses the performance of diurnal cycle of

precipitation from models available in both CMIP5 and CMIP6. Section 5 summarizes the main conclusion of this study.

2. Data

a. CMIP models

In this study, we analyze results from the Atmospheric Model Intercomparison Project (AMIP) simulations from 15 CMIP6 (Eyring et al. 2016) and 12 CMIP5 (Taylor et al. 2012) models. AMIP simulations follow a common experimental design, continuous across phases of CMIP, in which the observed sea surface temperature (SST) and sea ice amounts were prescribed in GCMs as lower boundary conditions. Consequently, the prescribed SST in AMIP simulations ensures that precipitation biases over the ocean are not associated with SST biases. We evaluate the period 1996–2005 in this study since this is the latest possible common decade between CMIP5 and CMIP6. Moreover, it has been shown that a stable diurnal cycle may be obtained with just a few years of data (e.g., Dai et al. 2007), which is also confirmed by our own sensitivity tests (not shown). Comparing model performance between the CMIP6 and CMIP5 models allows us to examine model improvements over the past several years.

The models used in this study are listed in Tables 1 and 2. We selected one model version from each modeling center that provides

TABLE 2. CMIP5 models used in this study. Models with CMIP6 counterparts are selected for further comparison (see text).

Models	Institute	CMIP6 counterpart	Horizontal grid size (lon × lat)	No. of vertical levels	References
ACCESS1.0	CSIRO and BoM, Australia	ACCESS-CM2	192 × 145	38	Bi et al. (2013)
BCC_CSM1.1-M	Beijing Climate Center, China	BCC_CSM2-MR	320 × 160	26	Wu et al. (2014)
BNU-ESM	Beijing Normal University, China		128 × 64	26	Ji et al. (2014)
CCSM4	NCAR		288 × 192	26	Neale et al. (2010)
CMCC-CM	Centro Euro-Mediterraneo sui Cambiamenti Climatici, Italy		480 × 240	31	Scoccimarro et al. (2011)
EC-Earth	ECMWF	EC-Earth3	320 × 160	62	Hazeleger et al. (2010)
FGOALS-g2	Institute of Atmospheric Physics, Chinese Academy of Sciences, China	FGOALS-g3	128 × 60	26	Li et al. (2013)
GFDL-HIRAM-C360	NOAA Geophysical Fluid Dynamics Laboratory		1152 × 720	32	Zhao et al. (2009)
HadGEM2-A	Met Office, United Kingdom		192 × 145	38	Collins et al. (2011)
INMCM4	Institute for Numerical Mathematics, Russia		180 × 120	21	Volodin et al. (2010)
IPSL-CM5A-LR	Institute Pierre-Simon Laplace, France	IPSL-CM6A-LR	96 × 96	39	Dufresne et al. (2013)
MIROC5	University of Tokyo, Japan	MIROC6	256 × 128	40	Watanabe et al. (2010)

3-hourly precipitation. Different model versions from the same center typically have little differences in diurnal and semidiurnal cycles (not shown). A few modeling centers have 3-hourly precipitation available in both CMIP6 and CMIP5: ACCESS-CM2 and ACCESS1.0; BCC_CSM2-MR and BCC_CSM1.1-M; EC-Earth3 and EC-Earth; FGOALS-g3 and FGOALS-g2; IPSL-CM6A-LR and IPSL-CM5A-LR; and MIROC6 and MIROC5 (see Tables 1 and 2 for model details). Comparing these models that appear in both CMIP6 and CMIP5 can help tracking performance changes in newer model versions, albeit with a smaller sampling size. In this study, we examine both the ensemble mean of all available models as well as the ensemble mean of those models that contribute to both CMIP6 and CMIP5.

b. Observations

Although there are many global products for precipitation measurements, only a few have subdaily temporal resolution (Sun et al. 2018). Three satellite-based products with subdaily temporal frequency are used in this study: the 3-hourly Tropical Rainfall Measuring Mission (TRMM) 3B42 version 7 data, the hourly Climate Prediction Center (CPC) Morphing technique (CMORPH)

bias-corrected product, and the 30-min Global Precipitation Measurement (GPM) Integrated Multisatellite Retrievals for GPM (IMERG). For selected regions, we also use ground-based rain gauge or radar measurements from long-term ARM sites for cross comparison. Table 3 provides an overview of the products used in this study. Although these products are available over different time periods, our composite analysis will demonstrate an encouraging level of consistency in their diurnal and semidiurnal cycle composites.

1) SATELLITE-BASED DATASETS

The TRMM 3B42 multisatellite product (Huffman et al. 2007) is a widely used 3-h rainfall product with 0.25° × 0.25° resolution covering 50°S to 50°N. It combines multiple satellite-based microwave precipitation estimates from low-Earth-orbit satellites and uses infrared (IR) estimates from geostationary satellites to fill data gaps in microwave estimates. At the final data-processing step, the 3-h data are scaled to sum to the monthly rain gauge product from the Global Precipitation Climatology Project (GPCP). This study uses the TRMM 3B42 data for the period from 1998 to 2013 archived by the Observations for Model Intercomparisons Project (Obs4MIPs; Waliser et al. 2020).

TABLE 3. Observation products. See text for acronym meanings.

Data	Time period	Spatial coverage	Horizontal resolution	Time resolution	Reference
TRMM 3B42 V7	1998–2013	50°S–50°N	0.25° × 0.25°	3 h	Huffman et al. (2007)
CMORPH_V1.0	1998–2018	60°S–60°N	0.25° × 0.25°	1 h	Joyce et al. (2004)
IMERG	2001–2018	90°S–90°N[a]	0.1° × 0.1°	30 min	Huffman et al. (2019)
ARMBE	SGP: 1993–2018 ENA: 2014–2018 TWPC2: 1998–2010 MAO: 2014–2015	Single point	Single point	1 h	Xie et al. (2010)
VARANAL	SGP: 2004–2016 MAO: 2014–2015	Single point	SGP: ~3° × 3° MAO: ~2° × 2°	SGP: 1 h MAO: 3 h	SGP: Xie et al. (2004); Tang et al. (2019) MAO: Tang et al. (2016)

[a] IR estimates are unavailable outside 60°S–60°N.

CMORPH (Joyce et al. 2004) is also a combination of PMW and IR satellite retrievals. However, unlike TRMM and IMERG that directly combine PMW and IR estimates, CMORPH only uses motion vectors of precipitating clouds from IR brightness temperature to propagate PMW retrievals. The final bias corrected CMORPH data are formed by combining forward- and backward-propagated PMW retrievals and calibrating with CPC gauge analysis over land and GPCP over ocean. There are three versions of CMORPH data with different temporal and spatial resolution at https://data.nodc.noaa.gov/cgi-bin/iso?id=gov.noaa.ncdc:C00948. In this study we use the version with 0.25° × 0.25° and 1-h resolution.

IMERG (Huffman et al. 2019) is designed to supersede the TRMM data with a much higher temporal (30 min) and spatial (0.1° × 0.1°) resolution. The operational algorithm is also changed. Instead of using IR estimates to infill passive microwave (PMW) maps, IMERG uses CMORPH-style wind vectors to advect microwave-observed precipitating areas, then applies a Kalman filter (Kalman 1960) to combine these maps and the IR estimates into a weighted estimate. As in TRMM 3B42, IMERG also uses GPCP ground-based data to scale the 30 min estimates to the monthly sum. Although IMERG data are available from 90°S to 90°N, poleward of 60°S and 60°N there are gaps in the analysis due to the unavailability of IR data.

2) GROUND-BASED DATASETS

In this study we select a few locations to further evaluate the diurnal cycle of precipitation in different climate regimes. Some of these locations coincide with the ARM long-term observational sites: the Southern Great Plains site (SGP), the Eastern North Atlantic site (ENA), the Tropical Western Pacific site C2 facility (TWPC2), and the Manacapuru site for the GOAmazon campaign (MAO). At these ARM sites, the available surface rain gauge measurements and/or radar retrievals provide additional information to validate satellite-based precipitation products and evaluate climate models. The ARM products used in this study are described below.

The ARM best estimate (ARMBE; Xie et al. 2010) data products are specifically tailored ARM measurements for the use in the evaluation of global climate models. They contain a best estimate of several atmosphere, cloud, and radiation quantities, including surface precipitation from in situ instruments such as rain gauge or optical rain gauge. The original precipitation measurements at the ARM sites are typically in 30-s or 1-min frequency. In the ARMBE data they are averaged into 1-h frequency for comparison with climate model output.

The ARM variational analysis (VARANAL) products (Zhang and Lin 1997; Zhang et al. 2001) are designed to provide the large-scale forcing fields for driving single-column version of climate models or cloud-resolving or large-eddy simulation models, but it also includes many important geophysical quantities (e.g., precipitation) that are often used in model evaluation. Unlike ARMBE, which uses single-point in situ rain gauge measurements, VARANAL uses ground-based radar data representing the average over a domain comparable to a GCM grid box. This study uses VARANAL products at two ARM sites: the continuous forcing data at SGP averaged over a ~370 km × 300 km domain (Tang et al. 2019;

Xie et al. 2004) and the forcing data at MAO averaged over a circle of 110 km in radius (Tang et al. 2016).

3) RECONCILING DIFFERENT TYPES OF PRECIPITATION MEASUREMENTS

Rain gauge observations are the most direct and accurate measurements of surface precipitation (Dai 2001; Dai et al. 2007; Sun et al. 2018; Xie and Arkin 1997), although measurement errors such as wind-induced low bias (e.g., Bowman 2005; Serra and McPhaden 2003) do exist. Rain gauge data are often available at high temporal resolution (e.g., 1 min) and long-term time coverage, but with poor spatial coverage. This single-point measurement may frequently miss precipitation events occurring nearby but not reaching the instrument location. When catching the precipitation, they typically measure much larger rainfall intensity than the area average. A single-point measurement becomes less representative of the region as the domain size increases (Bowman 2005), but the representation of a domain becomes more accurate when many rain gauges are averaged for long time period. In contrast, satellite measurements offer distinctly different strengths and weaknesses when compared to gauge data. They provide large and homogeneous spatial coverage, but with comparatively poor time sampling. IR measurements from geostationary satellites are usually needed to obtain subdaily information, as described in the previous subsection. Additionally, the indirect nature of the relationship between radiance measurements and precipitation, connected by an empirical retrieval algorithm, is the main source of data uncertainty.

The strengths and weaknesses of ground-based radar lie somewhere between those of single-point in situ measurements and satellite data. Ground-based radar provides coverage of a few hundred kilometers from the radar location with high-frequency sampling but is sparse over unpopulated areas. Like satellite measurement, the major error source of radar measurement is from the retrieval algorithm, which usually includes many uncertain assumptions and empirical relationships [e.g., see Villarini and Krajewski (2010) for a review of uncertainty in radar rainfall].

Previous studies have compared the diurnal cycle of precipitation from different types of measurements. Over most land areas, satellite products lag surface gauge-measured precipitation by a few hours (Dai 2006; Dai et al. 2007). This may be related to the fact that satellite instruments especially their IR measurements are more sensitive to high clouds such as cold anvil cirrus from deep convection but have difficulty in detecting warm low-cloud rainfall (Dai et al. 2007; Kikuchi and Wang 2008; Sorooshian et al. 2002; Zhao and Yatagai 2014). This lagging of diurnal phase in satellite measurements is not always true for all regions. Tian et al. (2005) compared GOES satellite-retrieved precipitation with surface station records over the United States and found that they are broadly consistent with each other. Gourley et al. (2010) compared TRMM 3B42 and another satellite product, Precipitation Estimation from Remotely Sensed Information Using Artificial Neural Networks (PERSIANN), with dense rain gauge measurements over Oklahoma in summer 2007 and found a 3–4-h-earlier nocturnal rainfall maximum in satellite data compared to rain gauge. They attributed this bias to the large cirrus shields associated with mesoscale convective
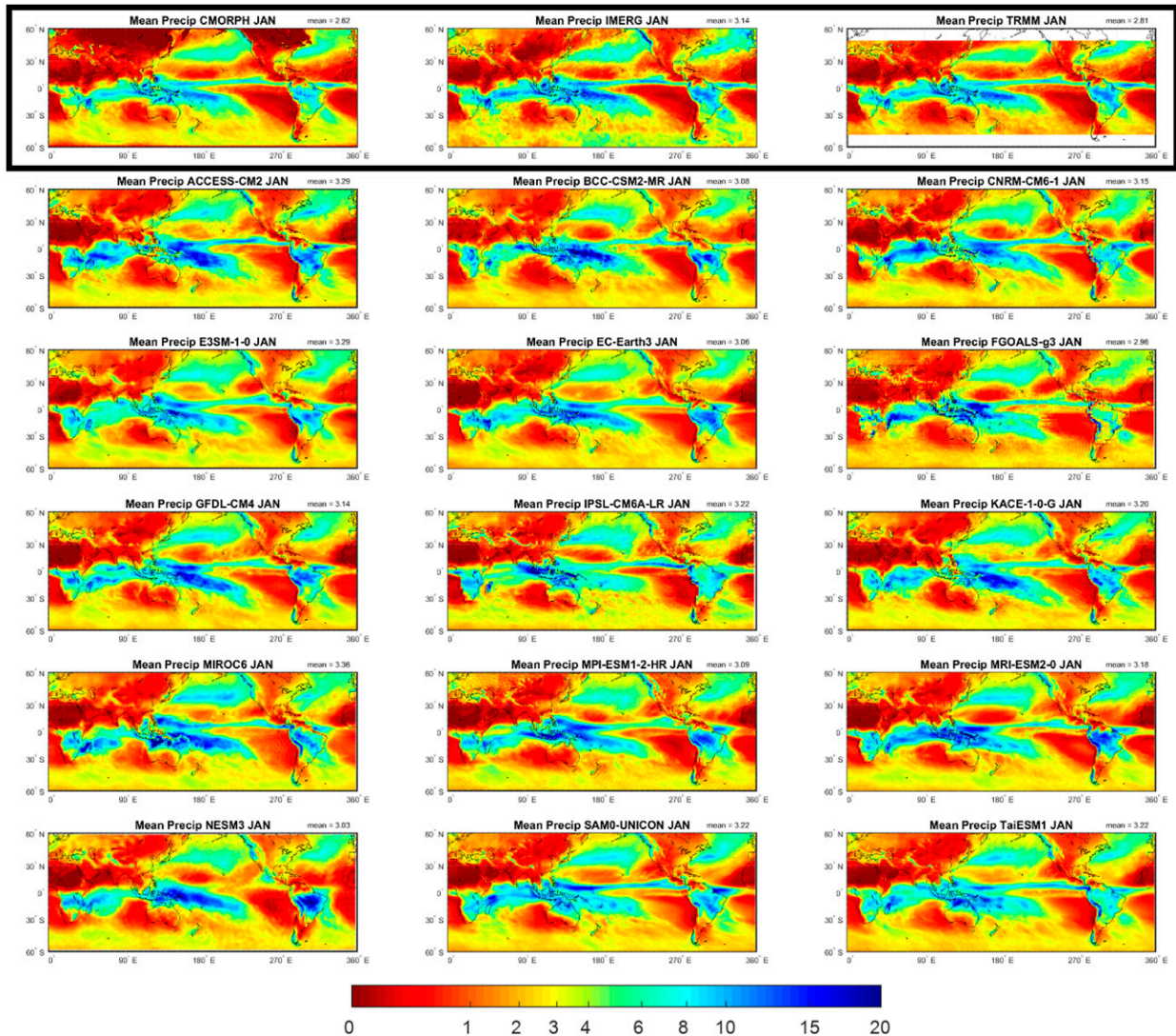
FIG. 1. Spatial distribution of mean precipitation (mm day^{-1}) in January from (top row) different satellite products and (bottom 5 rows) CMIP6 models. The value at the top-right corner in each panel is mean precipitation (mm day^{-1}) averaged from 60°S to 60°N (from 50°S to 50°N for TRMM).

systems (MCSs). Zhou et al. (2008) evaluated the PERSIANN and TRMM 3B42 datasets with gauge measurements over China for a 5-yr period and found that satellite may lead, be in phase with, or lag gauge data depending on the location of analysis. Surface-based precipitation radar may also have slight differences in the diurnal phase when compared to gauge data (Gourley et al. 2010; Liang et al. 2004; Santos e Silva et al. 2009), especially over high terrains (Nesbitt et al. 2008).

With these caveats in mind, we compare these three types of observational datasets in this study and use the results to guide the evaluation of the diurnal cycle of precipitation in CMIP models. As will be shown later, the satellite- and ground-based observations at the ARM locations in this study have good consistency in diurnal cycle, and in general the differences between these different classes of observational products are small in comparison to the large biases evident in climate models.

3. Results

Although our focus is on the diurnal and semidiurnal cycles of precipitation, it is important to first evaluate the overall performance of climatological mean of precipitation in CMIP models. After this baseline evaluation, we will examine the global pattern of diurnal and semidiurnal cycles and use diurnal harmonic polar plots to evaluate the model performance. The diurnal cycle of precipitation at 10 selected locations will then be examined using satellite and ground-based observations for cross validation.

a. Mean climate

Figures 1 and 2 compare the mean spatial pattern of precipitation from the three satellite products and CMIP6 models in January and July, respectively. The three observations are
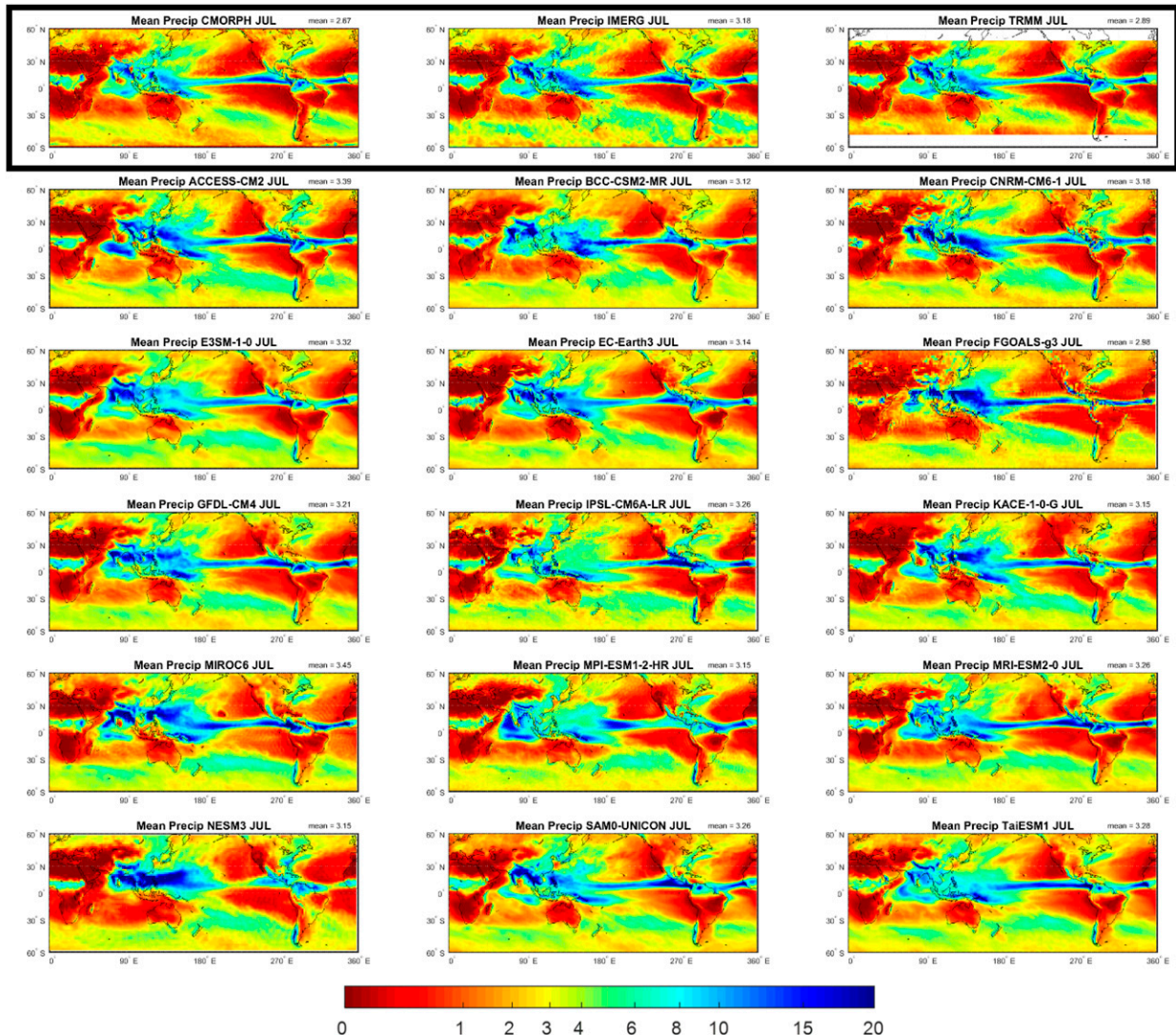
FIG. 2. As in Fig. 1, but for July.

consistent with each other in terms of the spatial pattern, except that CMORPH underreports the January precipitation over mid- and high-latitude land areas over Eurasia and North America. This has been recognized previously (e.g., Xie et al. 2017), and attributed to the poor capacity of the input PMW retrievals in detecting snowfall and cold season rainfall. Over the tropics, CMORPH data show slightly smaller rain rate than TRMM and IMERG. Note that although all three satellite products use PMW retrievals as the primary source of rain rate, the microwave measurement gaps in CMORPH are filled with propagating PMW retrievals while those in TRMM and IMERG are filled with IR estimates. The strong dependence of IR measurements with high clouds associated with deep convection may explain these differences.

Most CMIP6 models reproduce the broad patterns of precipitation in the observations, such as the intertropical convergence zone (ITCZ), the South Pacific convergence zone (SPCZ), and storm tracks as well as seasonal migration of

monsoon precipitation. However, some models have notable discrepancies with the observations. For example, in January, ACCESS-CM2, BCC_CSM2-MR, GFDL-CM4, MPI-ESM1.2-HR, MRI-ESM2.0, and NESM3 show wet bias over South America. FGOALS-g3 and IPSL-CM6A-LR underestimate precipitation over the SPCZ and South America. In July, CNRM-CM6.1 and FGOALS-g3 simulate stronger precipitation over the west Pacific and weaker precipitation over the central Africa. NESM3 shows strong precipitation from South Asia to the west Pacific without capturing the land–ocean contrast of the Asian monsoon precipitation.

The performance of the individual and the ensemble mean of CMIP6 models are shown as a Taylor diagram (Taylor 2001) in Fig. 3, with respect to IMERG data. Also shown are the ensemble mean of CMIP5 models and the other two satellite products. Diagrams quantify spatial characteristics between 50°S and 50°N over land and ocean, separately. CMORPH and TRMM are quite consistent with IMERG, with >0.95 spatial
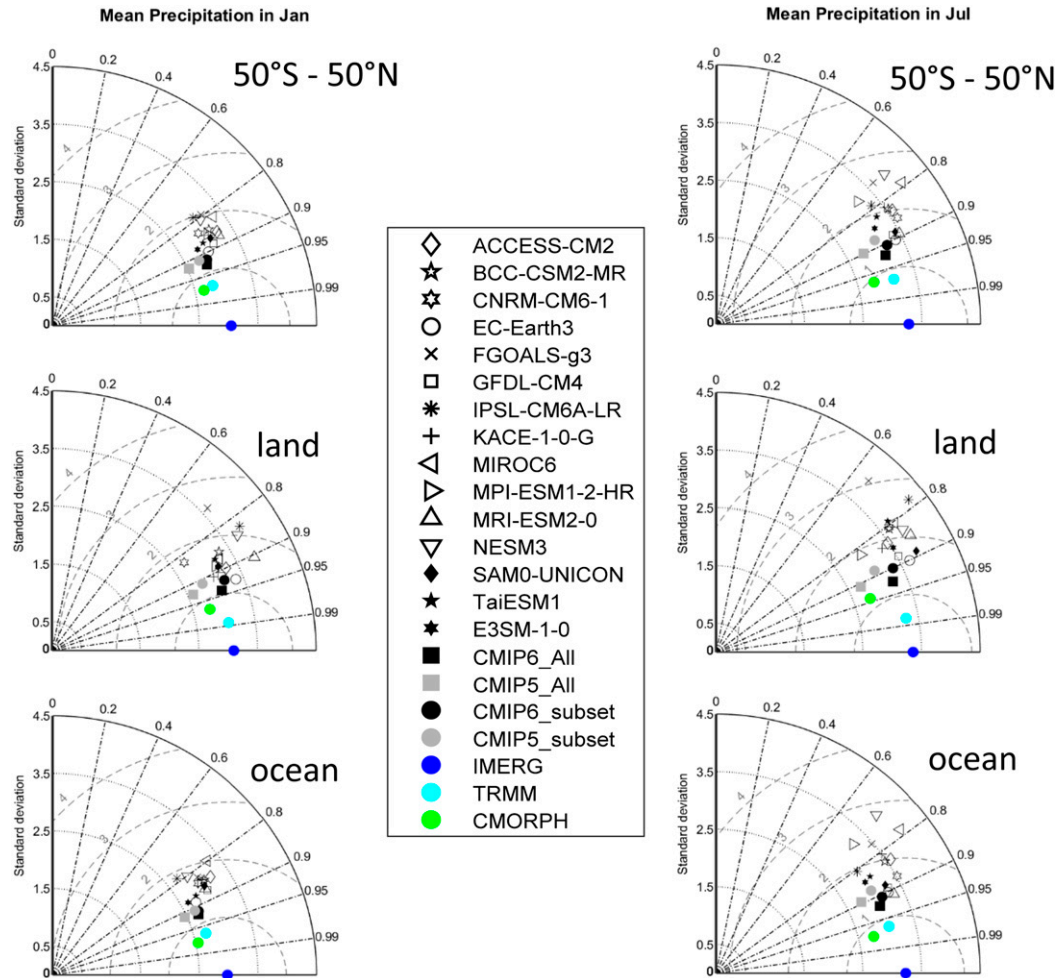
FIG. 3. Taylor diagram for mean precipitation (mm day^{-1}) with respect to IMERG data in (left) January and (right) July and for (top) all grids, (middle) land grids, and (bottom) ocean grids between 50°S and 50°N. All data are regridded into 2° × 2°. "CMIP6_subset" and "CMIP5_subset" are the ensemble mean of models with CMIP5/CMIP6 counterpart in Tables 1 and 2, respectively.

correlation coefficient and slightly smaller standard deviation. Most CMIP6 models have similar standard deviation and good correlation (between 0.7 and 0.9) with IMERG. Some models perform better over land, while some others perform better over ocean. The ensemble mean of the CMIP6 models outperforms the individual members and shows improvements (smaller distance to the reference point IMERG) compared to the ensemble mean of the CMIP5 models, both for all available models and the subset of models that participated in both CMIP5 and CMIP6. However, none of the individual models or the ensemble mean is as close to IMERG as TRMM or CMORPH. This suggests that despite improvements over the years, the model simulations still have pattern errors outside of observational error bounds.

b. Global distribution of diurnal precipitation

Because wintertime precipitation is more impacted by synoptic systems that have a smaller diurnal signal, we only focus on summertime (January for the Southern Hemisphere and July for the Northern Hemisphere) precipitation in this study. We apply Fourier analysis on the diurnal time series of precipitation as follows (Dai 2001):

$$F(t') = F_0 + S_1(t') + S_2(t') + \text{residual} \quad \text{and} \tag{1}$$

$$S_n(t') = A_n \sin(nt' + \sigma_n), \tag{2}$$

and consider the first two harmonic components: diurnal (S_1) and semidiurnal (S_2) cycles. In the above equations, F_0 is the mean value, A_n is the harmonic amplitude, σ_n is the phase, and t' is local solar time (LST) expressed in degrees or radians. Previous studies have shown that the diurnal and semidiurnal harmonics can well represent the daily variations of precipitation over most of the locations over the world (e.g., Dai 2001). The summertime diurnal harmonic amplitude ratio (amplitude normalized by mean precipitation) and phase (in LST) of precipitation for the three satellite
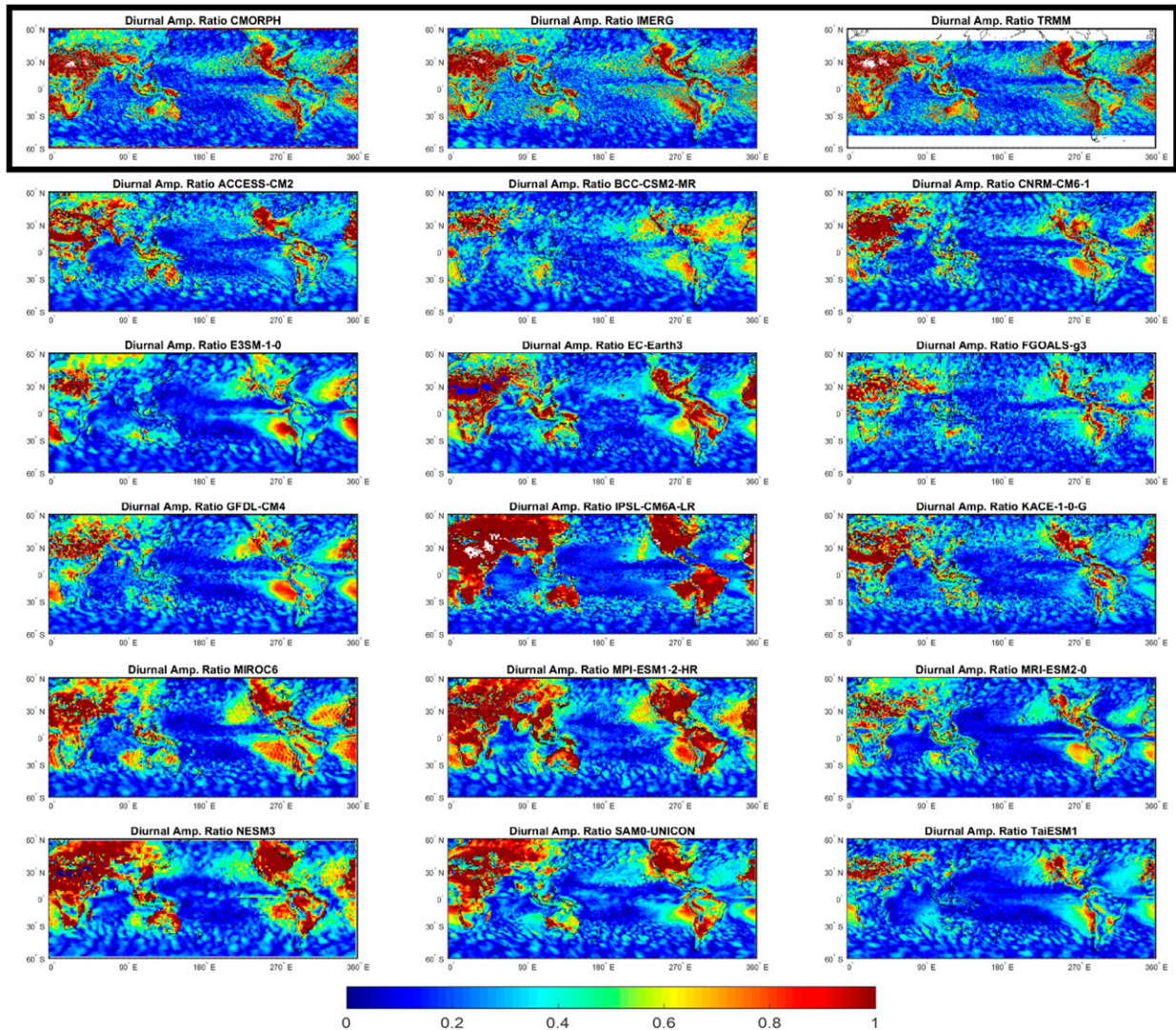
FIG. 4. Summertime (July in the Northern Hemisphere and January in the Southern Hemisphere) diurnal harmonic amplitude ratio (ratio of diurnal harmonic amplitude to monthly mean precipitation).

products and CMIP6 models are shown in Figs. 4 and 5, respectively.

In the observations, the amplitude ratio is saturated (>1) prominently over dry regions such as North Africa, the Middle East, the western part of North and South America, and the eastern part of the Pacific and the Atlantic Ocean, where the mean precipitation is small and contributed primarily by a few short-time events. Over other regions, the diurnal amplitude ratio ranges from 0.2 to 1 over land and typically below 0.6 over ocean. These broad diurnal amplitude characteristics in the state-of-the-art observational products used in this study are generally consistent with the data used in earlier studies (Dai et al. 2007). The observed diurnal phase shows a clear late afternoon peak over most land areas, with propagating systems regulating the phase over some regions such as the central United States, the Amazon region, and northern Argentina (e.g., a red to violet

to blue phase progression looking eastward over the central United States in the top panels of Fig. 5). Over the open ocean the observed diurnal phase generally peaks in the early morning, while over the southern Atlantic and many coastal areas including the Bay of Bengal, the South China Sea, the Gulf of Mexico, and the Caribbean, precipitation peaks in the daytime due to offshore propagation of convection (e.g., Aves and Johnson 2008; Yang and Slingo 2001).

CMIP6 models capture the amplitude ratio and phase over ocean fairly well, although some models (e.g., BCC_CSM2-MR, EC-Earth3, FGOALS-g3, MIROC6, and NESM3) peak several hours earlier. Over land, some models (IPSL-CM6A-LR, MPI-ESM1.2-HR, NESM3, and SAM0-UNICON) overestimate amplitude ratio. None of the models produce the peak as late as in the observations. E3SM-1.0, EC-Earth3, IPSL-CM6A-LR, MRI-ESM2.0, and SAM0-UNICON have relatively delayed diurnal peaks of ~1500 LST compared to other
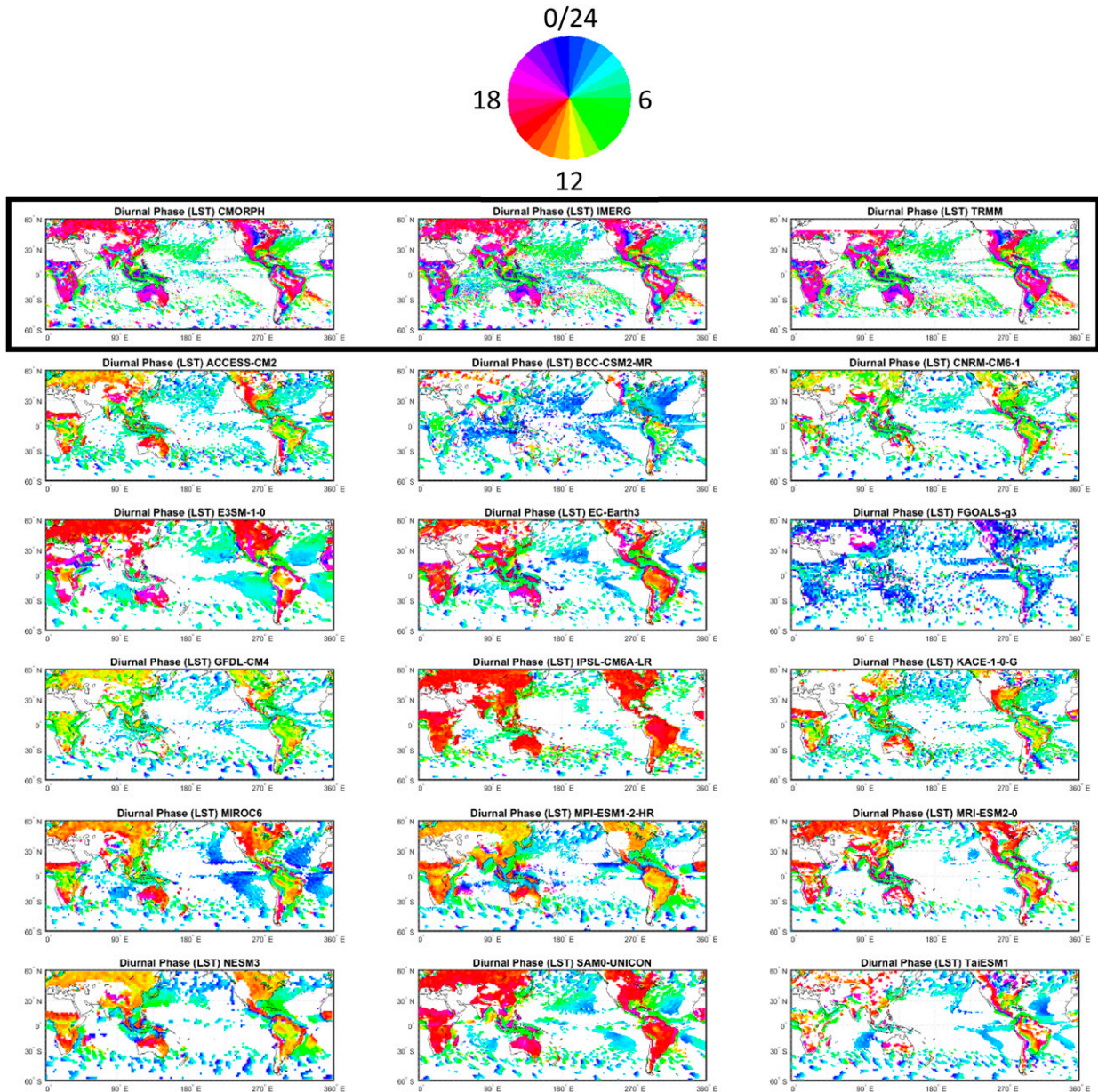
FIG. 5. As in Fig. 4, but for diurnal harmonic phase expressed as LST of maximum precipitation. Areas where either monthly mean precipitation is weaker than 0.75 mm day^{-1} or its diurnal amplitude ratio is weaker than 0.25 (Covey et al. 2016) are masked white.

models with peaks around noon, but they are still a couple hours early compared to the observations.

Over the central United States, the clear signal of observed nocturnal precipitation peak is a well-known feature that climate models have long had trouble capturing (Dai et al. 1999a; Dirmeyer et al. 2012; Lee et al. 2007b; Liang et al. 2004; Wang et al. 2015; Xie et al. 2019; Wang et al 2020). Observations have shown that the nocturnal peak primarily results from elevated convective systems associated with the eastward-propagating mesoscale convective systems originating over the Rocky Mountain range and decoupled from the surface (e.g., Geerts et al. 2017; Marsham et al. 2011; Xie

et al. 2014). Missing the mechanism to represent elevated convection in most cumulus parameterizations is one of the main reasons for the failure of capturing the nocturnal peak in many GCMs (Xie et al. 2019). In CMIP6, most models still have a problem capturing this propagation of precipitation, but a few models including BCC_CSM2-MR and TaiESM1 do capture the propagation signal over the central United States. A few other models (EC-Earth3, FGOALS-g3, and MRI-ESM2.0) show a nocturnal peak but without a propagation signal. More details about the nocturnal precipitation peak over the central United States and other locations will be discussed in section 3d.
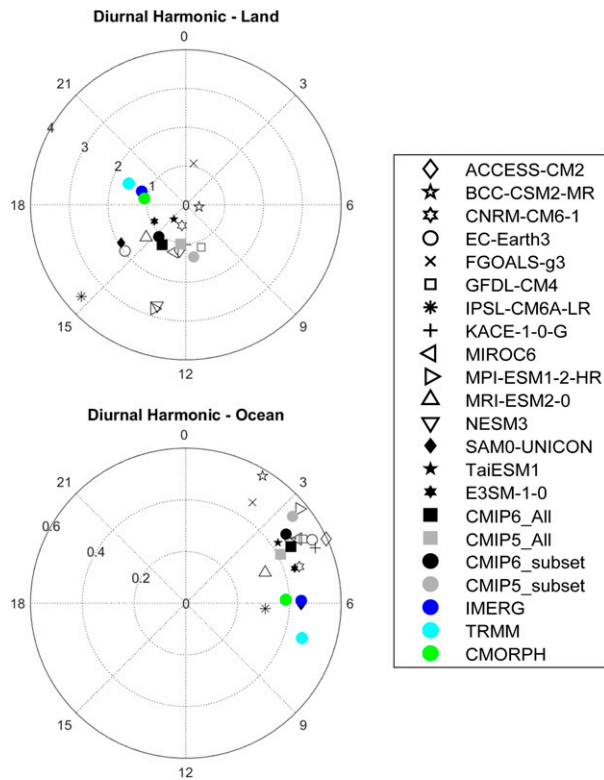
FIG. 6. Harmonic dial plots of summertime amplitude (mm day^{-1}) and phase of the first (diurnal) Fourier component averaged over land and ocean areas.

The overall performance of CMIP models in simulating the summertime diurnal cycle of precipitation is shown as harmonic dial plots (Covey et al. 2016) in Fig. 6. The radial distance from the origin represents the diurnal amplitude, with the angle representing the diurnal phase. The harmonic amplitude and phase are averaged over all land (ocean) points in summertime hemisphere between 50°S and 50°N using vector averaging. Covey et al. (2016) have shown that vector averaging is robust: it automatically downweights the areas with a weak diurnal cycle. The three observational products are consistent with each other, with only slight differences in amplitude and phase. Over land, observations show a late afternoon peak after 1800 LST, while most models show earlier phases between 1000 and 1600 LST with notable spread in amplitude. The CMIP6 ensemble mean shows improved phase over CMIP5 models, but is still 3 to 4 h earlier than observed. Five CMIP6 models have a diurnal peak after 1500 LST: IPSL-CM6A-LR, E3SM-1.0, EC-Earth3, SAM0-UNICON, and MRI-ESM2.0. However, different factors may to explain why these models have a diurnal peak closer to the observations over land. For example, EC-Earth3 modified the closure adjustment time scale and a coupling coefficient between the boundary layer and the free atmosphere to improve the diurnal phase (Bechtold et al. 2014); IPSL-6A-LR considered the preconditioning of deep convection by a phase of shallow cumulus convection and the self-maintenance of deep convection

through its interplay with cold pools, which are believed to be responsible for the diurnal cycle improvement (Hourdin et al. 2020; Rio et al. 2009); SAM0-UNICON applied an unified convective scheme that improve the diurnal cycle of precipitation through its ability to "simulate complex feedback processes among convective updrafts, convective downdrafts, and mesoscale organized flows and the interactions between subgrid and grid-scale processes" (Park 2014a,b). Over ocean, CMIP6 models have a smaller model spread than over land. The majority of models and the ensemble mean are 1 to 2 h earlier than observations. Exceptions include IPSL-CM6A-LR and SAM0-UNICON, which are consistent with observations in terms of both amplitude and phase.

c. Global distribution of semidiurnal precipitation

The second harmonic (semidiurnal cycle) amplitude ratio and phase of summertime precipitation are shown in Figs. 7 and 8, respectively, with harmonic dial plots in Fig. 9. Compared to the diurnal cycle, the observed semidiurnal cycle has a relatively weaker amplitude ratio except over dry regions where the mean precipitation is small and contributed primarily by a few short-time events. The semidiurnal phase is generally consistent among different satellite products, with the peak around 0400 LST over land, and around 0300 LST over ocean. These are consistent with the results from previous studies (Covey et al. 2016; Dai 2001; Dai et al. 2007).

Over land, some CMIP6 models such as EC-Earth3, IPSL-CM6A-LR, MPI-ESM1.2-HR, and NESM3, have a larger amplitude ratio than observations. E3SM-1.0, EC-Earth3, and SAM0-UNICON show a similar phase (after 0300 LST) to observations. Other models are a few hours earlier over land, with the ensemble mean peaks at ~0200 LST. The model spread is relatively larger in the semidiurnal cycle than the diurnal cycle, indicating larger uncertainty in semidiurnal signal. Nevertheless, the CMIP6 ensemble mean shows outperformance compared to CMIP5 ensemble mean. This is even more clear for those models where their performance can be tracked from CMIP5 to CMIP6. Over ocean the models are more consistent with each other and with the observations, despite some having smaller amplitudes. However, models have large spread in spatial distribution of the semidiurnal cycle over ocean, which also differs from the satellite products.

d. Diurnal cycle over selected locations

We select 10 locations around the world to further investigate the diurnal cycle of summertime precipitation over different climate regimes (July for the Northern Hemispheric and January for the Southern Hemispheric locations, except for TWPC2 that located at 0.5°N but to the south of the ITCZ, so January is used for TWPC2). All satellite observations are regridded into 2° × 2° in latitude and longitude. Although the diurnal cycle metrics are insensitive to spatial resolution, regridding helps to reduce the sampling error in high-resolution data (e.g., 0.1° in IMERG). These locations are selected because their diurnal cycles are relatively large and representative, and/or at ARM sites with long-term surface measurements. The 10 locations can be divided into three groups: the ARM ENA site, ARM TWPC2 site, and the southern Pacific
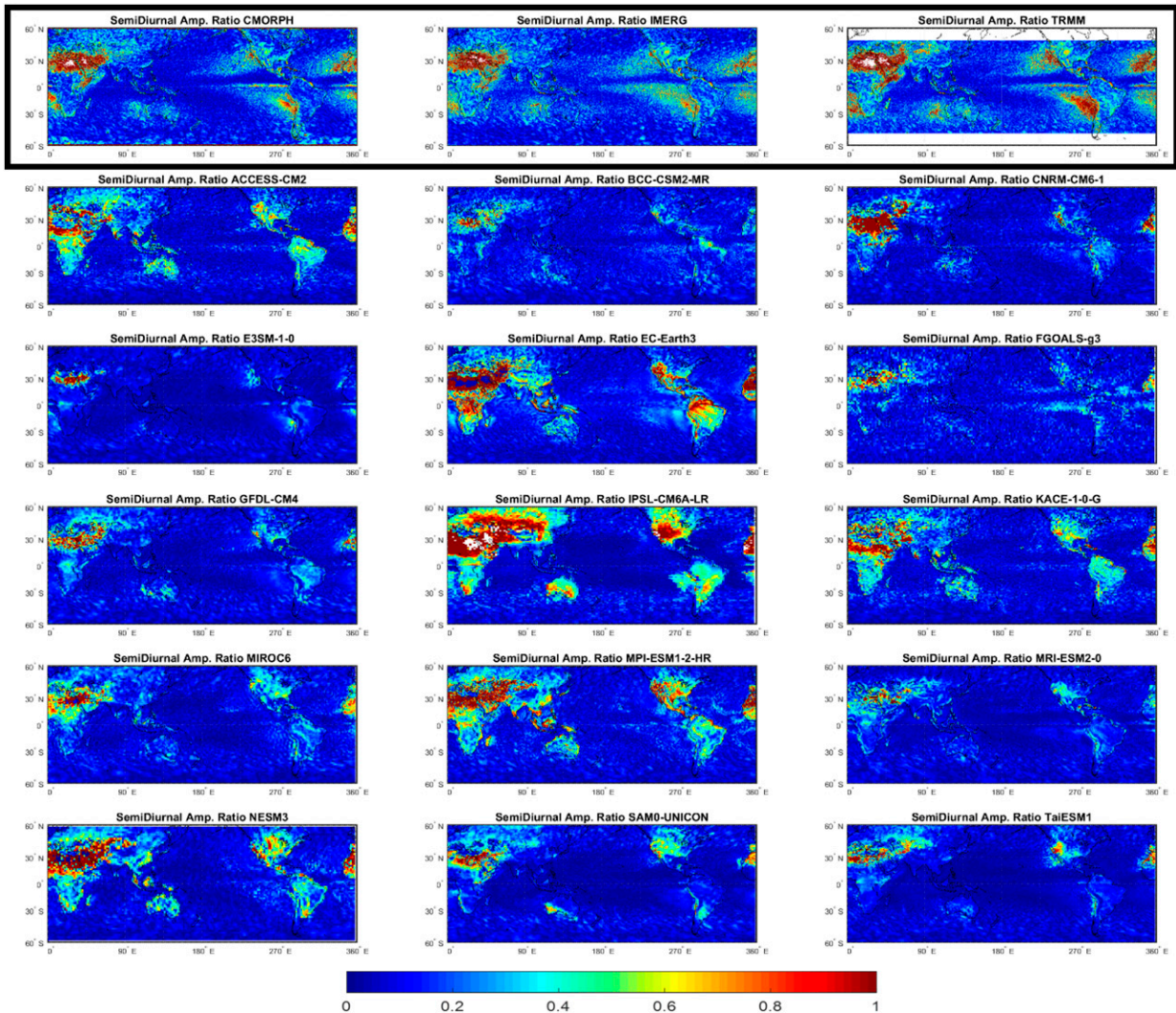
FIG. 7. As in Fig. 4, but for semidiurnal harmonic amplitude ratio.

(SPC) are locations representing oceans—although the two ARM sites are deployed on islands—with an early morning peak; India (IND), southeastern China (SEC), ARM MAO site, and southern Africa (SAF) are land points with an afternoon peak; the ARM SGP site, northern Argentina (NAR), and western Africa (WAF) are land points with a nocturnal peak.

Figure 10 shows the mean diurnal time series (dot) and the first harmonic component (line) of summertime precipitation from the 10 selected locations around the world. Figure 11 shows the first harmonic dial plots. Overall, the three satellite-based products and two surface-based products (when available) are in good consistency in the first harmonic, despite differences in the averaging time periods (Table 3). There are some site-specific uncertainties among the three satellite products on the mean value (e.g., SPC), amplitude (e.g., ENA) and phase (e.g., SAF). This is not unexpected since satellite data for individual small grid boxes can have larger errors than

averaged in a broad domain (e.g., Dai et al. 2007; Huffman et al. 2007; Joyce et al. 2004; Sorooshian et al. 2000). Although the ARMBE data have large high-frequency variation, likely due to its small sampling area as a point measurement, the diurnal harmonic is quite consistent with the collocated radar and satellite products. The consistency of these observational products from various sources builds confidence in using them to evaluate diurnal variability simulated by climate models.

The 10 locations represent the three typical features of diurnal cycle in observations: early morning peak over ocean, afternoon-to-early-evening peak over land, and nocturnal peak related to propagating convective systems. Over ocean points (ENA, TWPC2, and SPC) the observed diurnal cycles are relatively weak. The surface measurement (ARMBE) is consistent with the satellite products at ENA and TWPC2, although the instruments are located on small islands. CMIP6 models generally capture the early morning peak (cf. section 3b), but many of them underestimate the diurnal
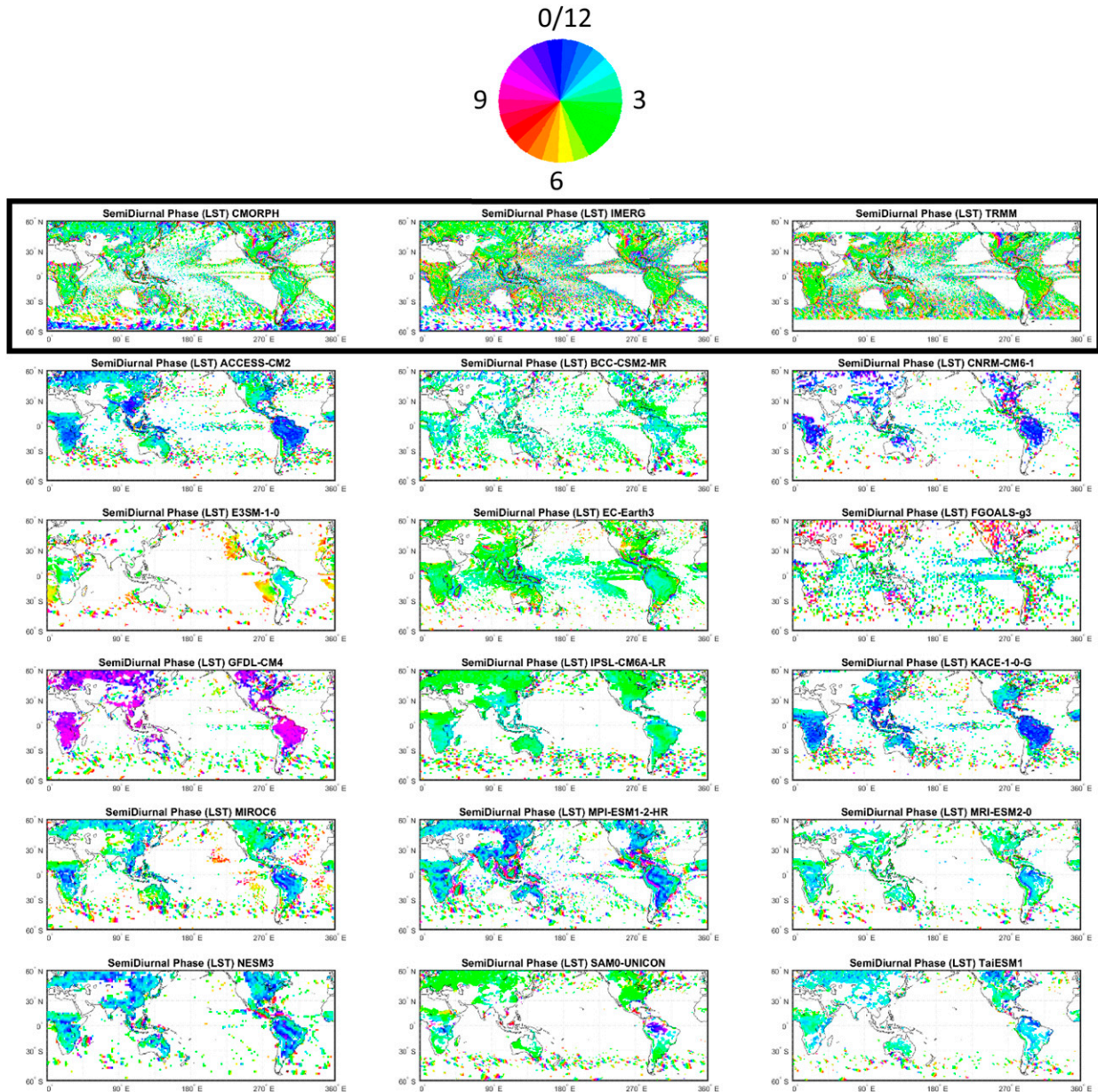
FIG. 8. As in Fig. 5, but for semidiurnal harmonic phase.

amplitude at TWPC2 and SPC and overestimate it at ENA (Fig. 11).

Over land points with an afternoon-to-early-evening precipitation peak (MAO, SAF, IND, and SEC), the CMIP6 ensemble mean peaks a few hours too early. However, the model spread is quite large in both amplitude and phase. EC-Earth3, E3SM-1.0, SAM0-UNICON, MRI-ESM2.0, and IPSL-CM6A-LR simulate diurnal phase close to the observations, although IPSL-CM6A-LR has an overly strong amplitude (this bias is also evident at large scales in Figs. 4 and 6). Significant improvements in the diurnal phase can be seen from CMIP5 to CMIP6 models, in which CMIP6 peaks are a few hours later

than CMIP5. These results are in agreement with the global analysis in section 3b. Also notable is the early afternoon peak at MAO. The diurnal cycle of precipitation over central Amazonia is the combined contribution of different types of convective systems (e.g., Greco et al. 1990; Tanaka et al. 2014; Tang et al. 2016), including propagating convective systems from the east coast of South America. Although some models produce an afternoon precipitation peak at MAO site, they may not be able to simulate all the mechanisms since they miss the propagating signal seen in observations (Fig. 5).

Over land points with a nocturnal precipitation peak (WAF, SGP, and NAR), the CMIP6 ensemble mean and most of its
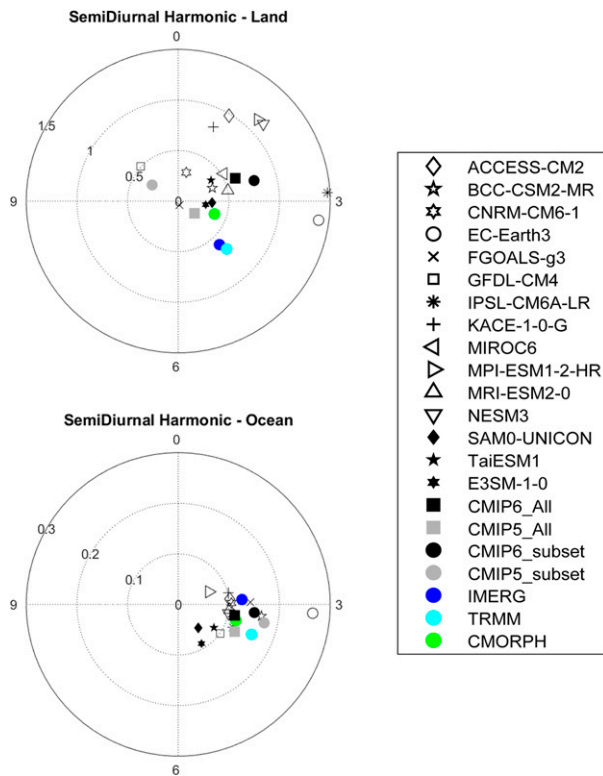
FIG. 9. As in Fig. 6, but for the second (semidiurnal) Fourier component.

members show a noon or afternoon peak rather than the observed nighttime peak. Only a few models capture the signal of nocturnal precipitation. At the north Argentina location, BCC_CSM2, EC-Earth3, and TaiESM1 are the only three models that capture well the nocturnal precipitation phase. This may be because all the three models allow convection to be triggered above the boundary layer (Bechtold et al. 2004; Lee et al. 2020; Wu 2012), which is found to be important in realistically simulating nocturnal elevated convection in GCMs (Wang et al. 2020; Xie et al. 2019). At SGP, only EC-Earth3 and FGOALS-g3 have a nocturnal precipitation peak between 1800 and 0600 LST, in agreement with the observed phase, albeit with weak amplitude. One must also note that FGOALS-g3 gives a nocturnal or early morning peak over most of the world's land regions, in disagreement with observations (Fig. 5). BCC_CSM2, MRI-ESM2.0, and TaiESM1 show an early morning peak around 0700 to 0800 LST. At WAF, FGOALS-g3 and GFDL-CM4 produce a precipitation peak around 0400 LST and EC-Earth3 produces a nocturnal precipitation peak around 2000 LST; all other models have a precipitation peak in the daytime. However, the performance of diurnal precipitation over western and central Africa is highly dependent on the choice of location, as the diurnal phase has large spatial variability (Fig. 5). This is primarily controlled by mesoscale convective systems that are often triggered over a few highlands in this region (Hodges and Thorncroft 1997; Rowell and Milford 1993; Yang and Slingo

2001) and propagate away from their source areas. The resolution used in the CMIP6 models is too coarse to resolve these mesoscale convective systems.

In additional to our diagnostic evaluation of the simulated diurnal cycle precipitation, we have quantified the consistency between models and observations with several large-scale objective performance metrics, including spatial characteristics in the form of Taylor diagrams (Fig. 3) and the amplitude/phase harmonic dial plots (Figs. 6 and 9). In Table 4 we provide several additional summary statistics quantifying the differences between models and the IMERG data for each of the selected location time series data included in Fig. 10. These include the root-mean-square difference (RMS) and its "centered" counterpart with the time mean removed from both the observations and models (RMSC). The former includes both bias and pattern error whereas the bias is removed from the later. Not surprisingly, the largest errors in Table 4 are for the IND location, with the bias making up an important contribution for many models. The bias dominates for several other locations including ENA and SPC. To further reveal the relationship between these objective summary statistics and the subpanels of Fig. 10, we provide (supplementary online material) interactive bar charts[1] that can be navigated to the underlying time series subpanel of Fig. 10. Absolute and relative (to other models) errors are readily shown in these online figures that also highlight the RMS and RMSC partitioning at each location. The performance metrics in this study will be incorporated into a benchmarking framework for simulated precipitation currently under development (Pendergrass et al. 2020).

The above analysis at selected locations further highlights the results of the global analysis: GCMs participating in the current CMIP6 project can capture the diurnal cycle of precipitation over ocean fairly well; a too-early peak of afternoon precipitation over land still exists but is improved over the CMIP5 models; most models (with a few exceptions) still cannot capture the nocturnal precipitation over land.

4. Tracking performance changes across model versions

A subset of the CMIP6 models are clearly identified as newer versions of a model contributed to CMIP5. In this section we further examine the diurnal cycle of precipitation in those models that are available in both CMIP6 and CMIP5: ACCESS-CM2 and ACCESS-1.0, BCC_CSM2-MR and BCC_CSM1.1-M, EC-Earth3 and EC-Earth, FGOALS-g3 and FGOALS-g2, IPSL-CM6A-LR and IPSL-CM5A-LR, and MIROC6 and MIROC5. Figures 12 and 13 show the diurnal harmonic amplitude ratio and phase, respectively, for these model pairs; Fig. 14 shows the corresponding harmonic dial plots.

Among the six model pairs, three of them (ACCESS, FGOALS, and MIROC) have no or minor improvement on their physical parameterizations for cumulus convection from their CMIP5 to CMIP6 version (Bi et al. 2013; Li et al. 2020;

---

[1] https://pcmdi.llnl.gov/pmp-preliminary-results/interactive_plot/precip/diurnal/pr_diurnal.cycle_rms.bar_all.loc.mod_interactive.html.
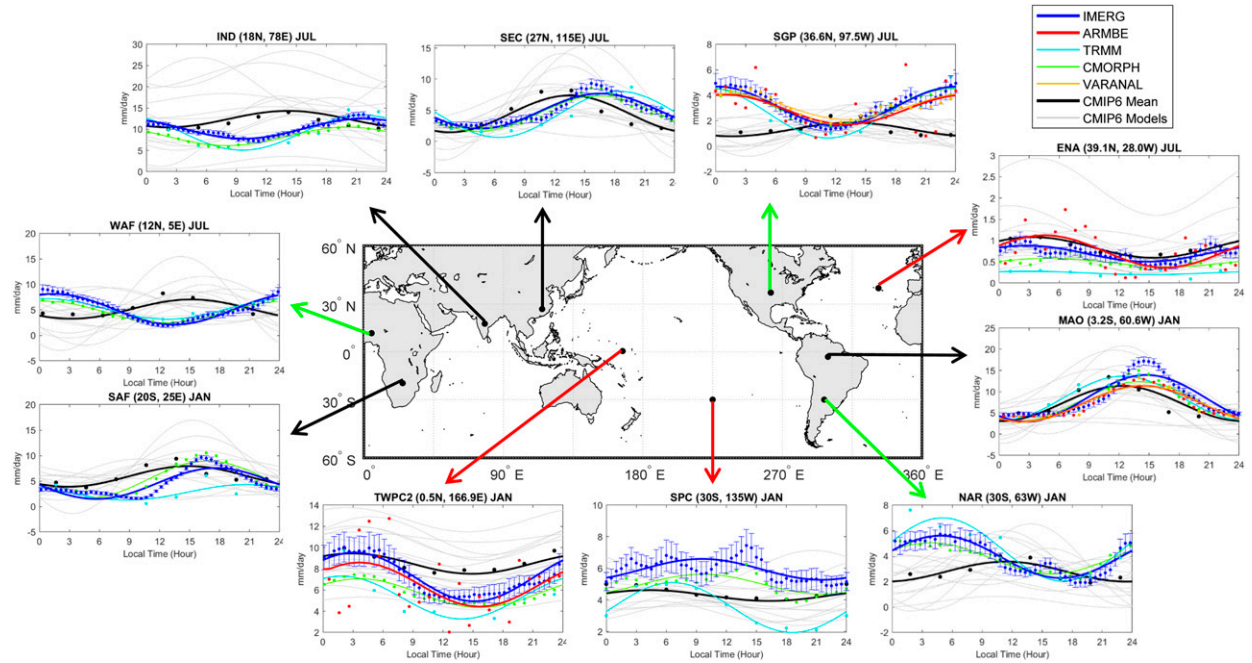
FIG. 10. Summertime mean diurnal cycle of precipitation (dot) and the first Fourier component (line) for 10 selected locations. One standard error bar is shown for IMERG data. The colors of the arrows pointing from the locations represent the different types of diurnal cycle: black represents afternoon peak over land, red represents morning peak over ocean, and green represents nocturnal peak over land.

Tatebe et al. 2019; Walters et al. 2019). Therefore, their diurnal cycles are basically unchanged from CMIP5 to CMIP6. The other three (BCC_CSM, EC-Earth, and IPSL) documented notable modifications in their cumulus parameterizations that contribute to the improvement of diurnal cycle of precipitation,

as discussed below. This further suggests that the model errors in the diurnal cycle of precipitation can be related to deficiencies in representing convection in climate models.

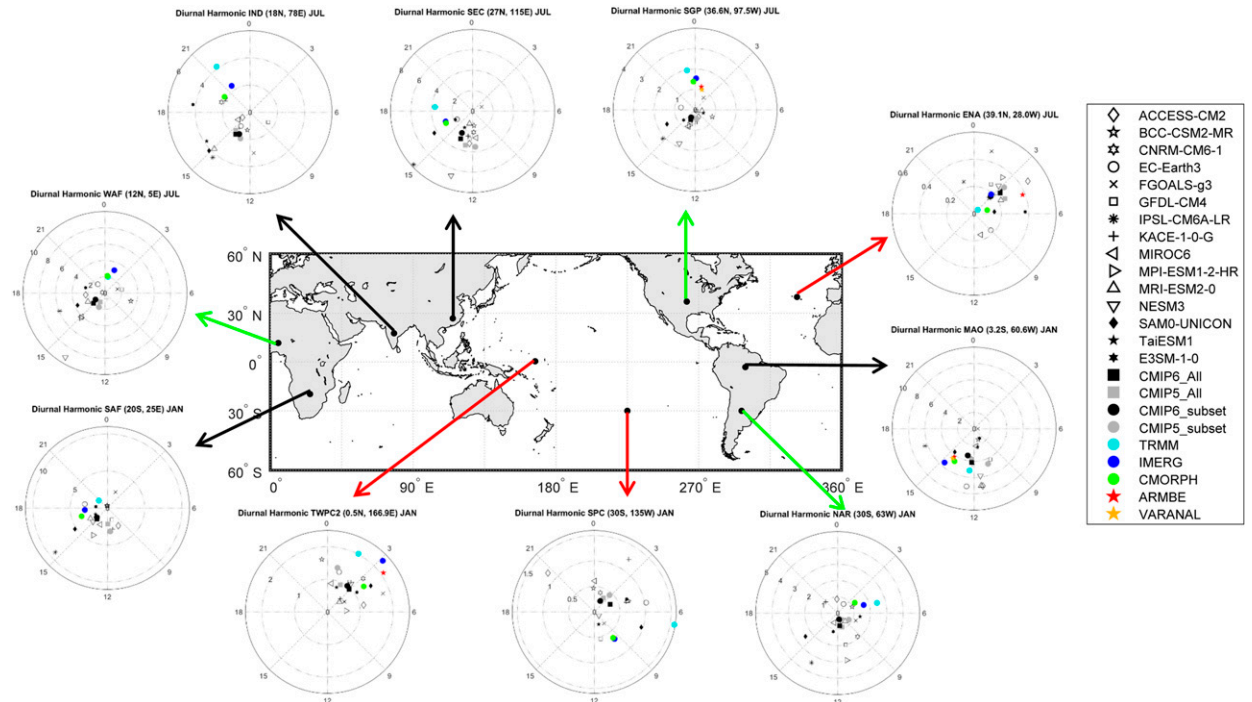BCC_CSM modified its convective triggering function from the relative humidity threshold in BCC_CSM1.1-M to

FIG. 11. Harmonic dial plots of the first Fourier component of summertime precipitation over the 10 selected locations. The unit of amplitude is mm day^{-1}.

TABLE 4. Uncentered (RMS; left column) and centered (RMSC; right column) root-mean-square difference of first diurnal harmonics shown in Fig. 10 for each CMIP6 model. The RMS and RMSC are obtained against the IMERG data. Boldface and italic indicate high and low RMS/RMSC, respectively, based on one standard deviation in each column.

	IND		SEC		SGP		WAF		ENA		MAO		SAF		TWPC2		SPC		NAR	
	RMS	RMSC	RMS	RMSC	RMS	RMSC	RMS	RMSC	RMS	RMSC	RMS	RMSC	RMS	RMSC	RMS	RMSC	RMS	RMSC	RMS	RMSC
ACCESS-CM2	9.48	1.77	2.30	2.24	*1.55*	1.37	3.43	3.26	0.33	0.20	4.75	3.83	3.96	*3.46*	1.67	1.05	*1.30*	*1.30*	1.31	1.15
BCC_CSM2-MR	4.48	2.48	2.14	1.93	2.54	1.46	3.16	3.06	0.13	**0.02**	6.88	3.50	2.46	2.10	1.31	*1.29*	1.77	0.77	1.78	**0.49**
CNRM-CM6.1	**2.79**	**1.01**	2.64	2.03	2.32	1.15	2.69	2.20	*1.62*	*0.34*	3.27	2.29	3.22	2.12	3.34	**0.57**	**1.06**	0.68	1.43	1.42
E3SM-1.0	3.76	2.19	**1.58**	**0.67**	2.20	1.53	3.21	2.88	0.22	0.20	3.65	3.65	3.34	1.07	**0.92**	0.89	1.89	0.58	2.43	1.74
EC-Earth3	2.99	2.18	2.47	0.78	2.06	1.15	3.21	1.86	0.41	0.19	2.86	2.80	**0.62**	**0.56**	2.45	0.95	2.34	0.67	**1.03**	0.85
FGOALS-g3	12.88	3.74	4.09	2.64	**1.78**	**0.73**	**2.25**	**1.71**	0.70	*0.23*	7.12	4.09	3.41	3.35	*3.91*	**0.73**	1.33	0.26	1.35	0.77
GFDL-CM4	7.16	2.68	2.09	2.04	3.07	1.54	2.89	1.82	0.30	0.05	4.68	3.88	2.67	2.67	5.42	0.84	**0.38**	**0.19**	1.99	1.91
IPSL-CM6A-LR	*14.41*	3.91	4.52	3.74	3.10	2.40	6.01	5.86	0.16	0.15	2.96	**2.21**	5.79	4.93	2.83	1.22	2.63	**0.02**	3.50	*3.36*
KACE-1.0-G	8.42	2.30	1.97	1.84	2.36	1.54	2.64	2.64	0.25	**0.02**	2.82	2.31	3.29	3.19	1.24	1.23	1.27	*1.14*	2.01	1.61
MIROC6	3.70	1.82	2.87	2.36	2.90	1.72	5.02	4.96	0.31	0.22	3.99	3.04	2.35	2.02	2.08	1.19	1.68	0.86	1.62	1.47
MPI-ESM1.2-HR	7.14	7.07	5.34	5.32	3.02	1.67	5.32	5.04	0.17	0.11	5.48	5.45	2.68	2.57	1.37	1.35	2.70	0.57	2.74	2.54
MRI-ESM2.0	4.84	3.45	2.18	1.62	2.56	1.17	3.69	3.56	0.14	0.06	5.62	3.70	3.86	**0.98**	*3.91*	1.29	1.89	0.56	2.71	1.07
NESM3	*11.52*	5.40	3.86	3.85	3.00	2.37	8.76	8.73	0.18	0.06	4.57	3.25	1.71	1.37	**0.98**	0.84	2.45	0.39	3.77	1.17
SAM0-UNICON	3.80	3.62	**1.35**	1.13	2.53	1.90	5.09	4.39	0.09	0.09	**1.27**	**1.27**	4.52	2.08	3.15	**0.61**	2.61	0.40	3.36	2.82
TaiESM1	3.22	3.19	2.92	1.35	2.30	1.25	3.11	3.09	0.13	0.06	3.11	3.11	2.19	1.08	1.17	1.14	2.38	0.30	**0.55**	**0.54**

the vertical velocity threshold in BCC_CSM2-MR. It also slightly changed the calculation of the lifting condensation level. Wu et al. (2019) found that these modifications improved the diurnal cycle of precipitation over China. Globally, BCC_CSM2-MR also shows delayed diurnal phase from ~0300 to ~0600 LST comparing to BCC_CSM1.1-M over land such as East Asia, the east United States, Africa, and South America (Fig. 13). However, the diurnal peak is still out of phase in comparison to the observations and no improvement is seen over ocean.

EC-Earth3 modified the convective adjustment time scale and a coupling coefficient α between the boundary layer and the free troposphere in its convective closure (Bechtold et al. 2014). Although Bechtold et al. (2014) state that this approach is pragmatic and "we do not yet know if this closure and the parameter range for α indeed reflect the actual physical coupling between the boundary layer and the deep convection," the diurnal cycle over land is significantly improved with the phase shifting from noon in EC-Earth to after 1500 LST in EC-Earth3. This result and a recent study by Yang et al. (2020) indicate that the coupling among boundary layer, shallow convection, and deep convection in a climate model could largely impact the simulated diurnal cycle of precipitation.

IPSL also shows clear improvement of diurnal phase from its CM5A to CM6A, both over land and over ocean. The new convective parameterization in IPSL-CM6A includes a comprehensive interaction between the boundary layer shallow convection, deep convection, and cold pools. The consideration of preconditioning of deep convection by shallow convection and the effect of cold pools to the self-maintenance of deep convection are believed to be responsible for the diurnal cycle improvements (Hourdin et al. 2020; Rio et al. 2009). Overall, with the contribution from these individual models, the ensemble mean performance of diurnal cycle of precipitation is improved (Fig. 6).

5. Summary and discussion

GCMs have shown persistent problems in representing the diurnal cycle of precipitation through many years of model development. These problems include 1) too-early precipitation peak over ocean with the observed peak in the early morning, 2) too-early precipitation peak over land with the observed peak in the late afternoon, and 3) missing nocturnal precipitation peak over some regions. With the evaluation of precipitation in the AMIP simulations from the recently released CMIP6 models, we found that most of the CMIP6 models are still suffering from these problems.

Nevertheless, substantial improvements have been made in CMIP6 models compared to CMIP5 versions. Over land, most of the CMIP5 models have precipitation "phased locked" to insolation with a peak at or near noontime, while in CMIP6 many models have delayed their precipitation peak over land, leading to an improved diurnal phase in the ensemble mean. Better treatments of the interactions between convection and boundary layer processes (e.g., Hourdin et al. 2020; Park 2014a,b) and more sophisticated convective triggering and closure functions (e.g., Bechtold et al. 2014) contribute to this
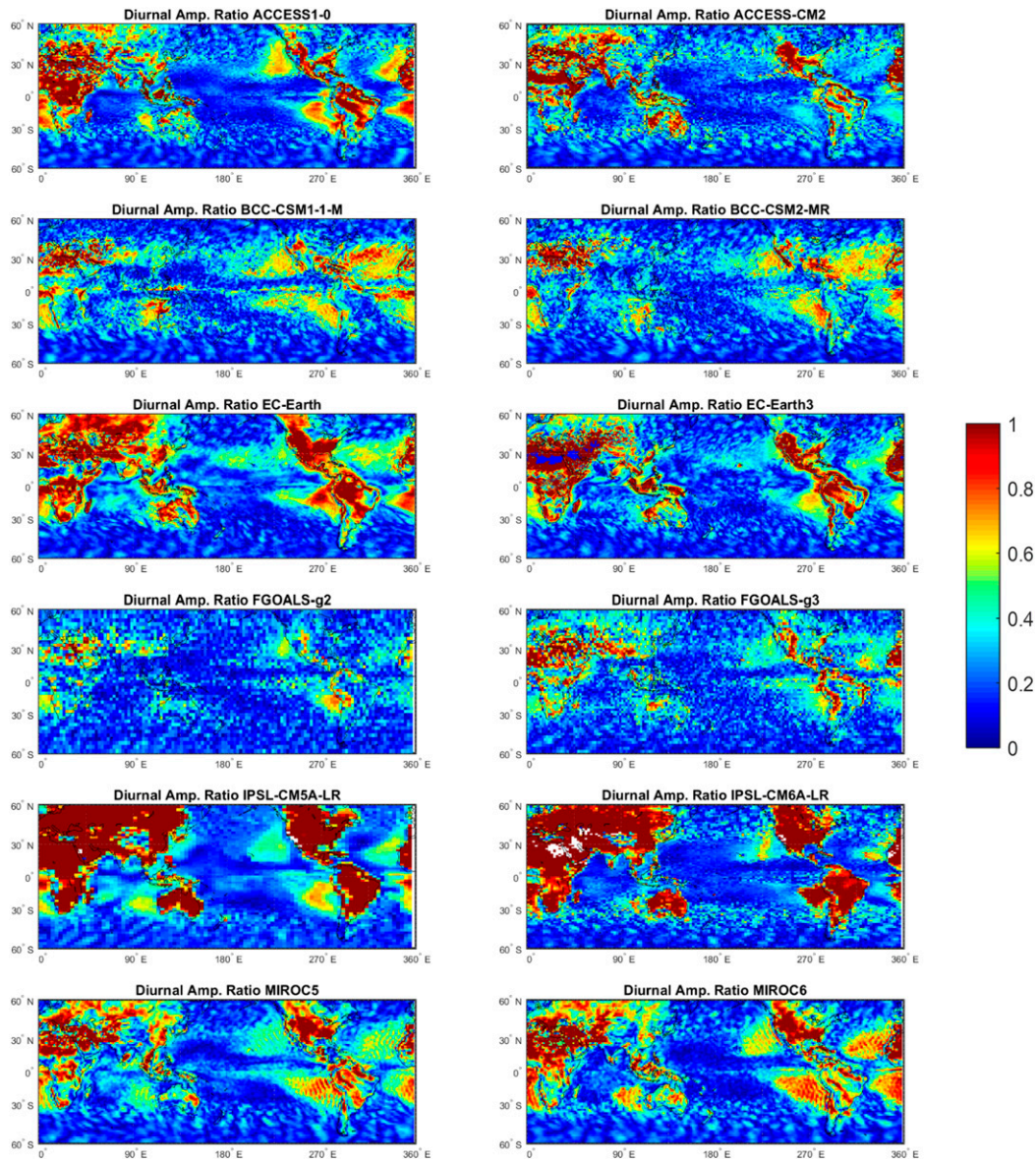
FIG. 12. Summertime diurnal harmonic amplitude ratio from the subset of models that appear in both (left) CMIP5 and (right) CMIP6.

improvement. Nocturnal precipitation peaks over certain regions, however, are still missing in most CMIP6 models. A few models can capture this facet of the observations, but the simulated peak time varies. One common feature of the more successful models is that they all allow convection to be triggered above the boundary layer (Bechtold et al. 2004; Wang et al. 2015; Wu 2012), indicating the importance of the capability to capture midlevel convection for climate models to simulate nocturnal precipitation peaks. In line with this, a recent work by Xie et al. (2019) proposed a new convective trigger that emulates collective dynamical effects that prevent convection from being triggered too frequently and allows air parcels to launch above the boundary layer to capture

nocturnal elevated convection to improve the modeling of diurnal cycle of precipitation. Testing of this new trigger in the E3SM atmospheric model version 1 (Rasch et al. 2019; Xie et al. 2018) showed that it can significantly improve the diurnal cycle of precipitation without degrading the mean climatology. The observed nocturnal peaks in the central United States, Maritime Continent, and Amazon can be well captured with the new trigger. It should be noted that the nocturnal precipitation events over these regions are primarily associated with the propagation of MCSs that results from moist conditionally unstable layers located above the stable boundary layer at night. Given the resolution used in current climate models, the propagating MCSs cannot be resolved and are poorly
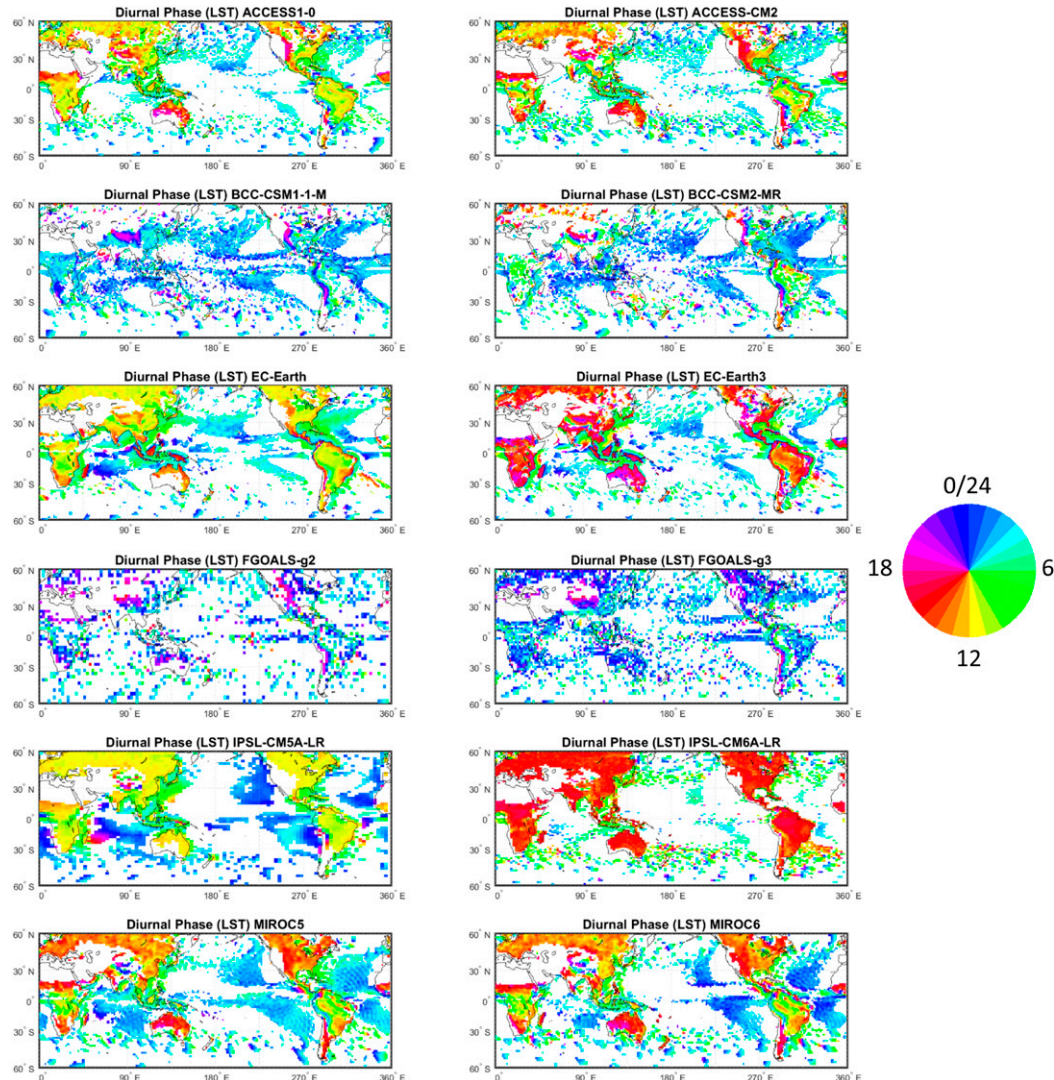
FIG. 13. As in Fig. 10, but for diurnal harmonic phase.

simulated. Allowing convection to be triggered above the boundary layer is one way for climate models to detect the middle level atmospheric instability caused by propagating MCSs and thereby they can capture the resulting nocturnal precipitation. Other ongoing efforts include the introduction of convective memory (i.e., a prognostic variable, such as the cold pools and mesoscale organized flows in the boundary layer) in convective parameterizations (e.g., Davies et al. 2009; Mapes and Neale 2011; Pan and Randall 1998; Park 2014a; Rio et al. 2009) to capture the propagation of convection.

Uncertainty of precipitation measurements at diurnal and subdiurnal time scales is a continuing concern in comparing climate models with observations. This study used three satellite-based products covering global tropics and subtropics together with two types of ground-based measurements at selected locations. Although all observations are subject to uncertainties as discussed in section 2b(3), we have shown that

these observational datasets used here are consistent in diurnal and semidiurnal cycles. Therefore, these observations can serve as suitable references for evaluation of the precipitation diurnal cycle in climate models.

The semidiurnal cycle is usually weaker than diurnal cycle. Moreover, the consistency between different observational products and between observations and models is notably less than for the diurnal cycle. This is partly due to the signal processing limits in the mathematical calculation of Fourier analysis. Although satellite products are now available in 1-h or half-hour frequency, CMIP6 models are still archived in 3-h frequency. With 3-hourly data, the semidiurnal harmonic has only four time points per cycle, which has large uncertainties, while harmonic analysis with higher frequency will add little real information since the limiting Nyquist period is 6 h. Increasing the temporal resolution from 3 h to higher frequency (e.g., 1 h or 30 min) in the CMIP data will reduce the
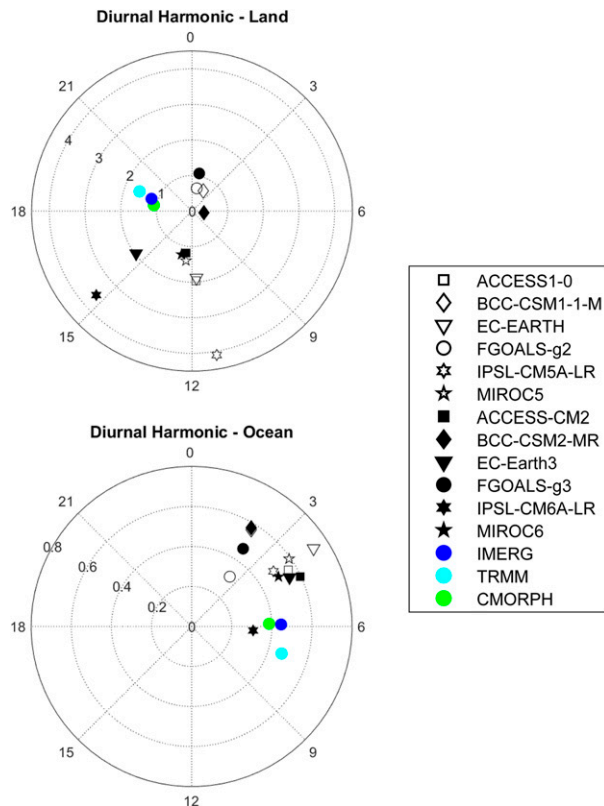
FIG. 14. The diurnal harmonic dial plots of the summertime precipitation from the models that appear in both CMIP5 and CMIP6 averaging over land and ocean areas. The unit of amplitude is mm day^{-1}.

sampling errors and help the evaluation of semidiurnal cycle and other subdiurnal variabilities such as intermittency (Covey et al. 2018; Trenberth et al. 2017).

CMIP6 is still ongoing and it is expected that more simulations with new models will be contributed over the next several years. Via a concerted effort to advance the benchmarking of simulated precipitation, the performance metrics (and underlying diagnostics) from our study will be updated online to include newer model contributions to CMIP6. Moreover, our emphasis in this study is on the composite diurnal and semidiurnal composite averaged across a decade. Our sensitivity tests confirm earlier studies that a decade is sufficient for robustly isolating the solar forced diurnal cycle from longer time scale unforced variations including dominant interannual variability such as El Niño. Accurate representation of unforced precipitation variability needs to be examined across time scales and is currently ongoing, but is beyond the scope of this study.

REFERENCES

Aves, S., and R. H. Johnson, 2008: The diurnal cycle of convection over the northern South China Sea. *J. Meteor. Soc. Japan*, **86**, 919–934, https://doi.org/10.2151/jmsj.86.919.

Bechtold, P., J.-P. Chaboureau, A. Beljaars, A. K. Betts, M. Köhler, M. Miller, and J.-L. Redelsperger, 2004: The simulation of the diurnal cycle of convective precipitation over land in a global model. *Quart. J. Roy. Meteor. Soc.*, **130**, 3119–3137, https://doi.org/10.1256/qj.03.103.

——, N. Semane, P. Lopez, J.-P. Chaboureau, A. Beljaars, and N. Bormann, 2014: Representing equilibrium and nonequilibrium convection in large-scale models. *J. Atmos. Sci.*, **71**, 734–753, https://doi.org/10.1175/JAS-D-13-0163.1.

Betts, A. K., and C. Jakob, 2002: Study of diurnal cycle of convective precipitation over Amazonia using a single column model. *J. Geophys. Res.*, **107**, 4732, https://doi.org/10.1029/2002JD002264.

Bi, D., and Coauthors, 2013: The ACCESS coupled model: Description, control climate and evaluation. *Aust. Meteor. Oceanogr. J.*, **63**, 41–64, https://doi.org/10.22499/2.6301.004.

Bowman, K. P., 2005: Comparison of TRMM precipitation retrievals with rain gauge data from ocean buoys. *J. Climate*, **18**, 178–190, https://doi.org/10.1175/JCLI3259.1.

Burleyson, C. D., Z. Feng, S. M. Hagos, J. Fast, L. A. T. Machado, and S. T. Martin, 2016: Spatial variability of the background diurnal cycle of deep convection around the GoAmazon2014/5 field campaign sites. *J. Appl. Meteor. Climatol.*, **55**, 1579–1598, https://doi.org/10.1175/JAMC-D-15-0229.1.

Byun, Y.-H., Y.-J. Lim, H. M. Sung, J. Kim, M. Sun, and B.-H. Kim, 2019: NIMS-KMA KACE1.0-G model output prepared for CMIP6 CMIP AMIP. Earth System Grid Federation, accessed 17 June 2020, https://doi.org/10.22033/ESGF/CMIP6.8350.

Cao, J., and Coauthors, 2018: The NUIST Earth System Model (NESM) version 3: Description and preliminary evaluation. *Geosci. Model Dev.*, **11**, 2975–2993, https://doi.org/10.5194/gmd-11-2975-2018.

Carbone, R. E., J. D. Tuttle, D. A. Ahijevych, and S. B. Trier, 2002: Inferences of predictability associated with warm season precipitation episodes. *J. Atmos. Sci.*, **59**, 2033–2056, https://doi.org/10.1175/1520-0469(2002)059<2033:IOPAWW>2.0.CO;2.

Collins, W. J., and Coauthors, 2011: Development and evaluation of an earth-system model—HadGEM2. *Geosci. Model Dev.*, **4**, 1051–1075, https://doi.org/10.5194/gmd-4-1051-2011.

Covey, C., P. J. Gleckler, C. Doutriaux, D. N. Williams, A. Dai, J. Fasullo, K. Trenberth, and A. Berg, 2016: Metrics for the diurnal cycle of precipitation: Toward routine benchmarks for climate models. *J. Climate*, **29**, 4461–4471, https://doi.org/10.1175/JCLI-D-15-0664.1.

——, C. Doutriaux, P. J. Gleckler, K. E. Taylor, K. E. Trenberth, and Y. Zhang, 2018: High-frequency intermittency in observed and model-simulated precipitation. *Geophys. Res. Lett.*, **45**, 12 514–512 522, https://doi.org/10.1029/2018GL078926.

Dai, A., 2001: Global precipitation and thunderstorm frequencies. Part II: Diurnal variations. *J. Climate*, **14**, 1112–1128, https://doi.org/10.1175/1520-0442(2001)014<1112:GPATFP>2.0.CO;2.

——, 2006: Precipitation characteristics in eighteen coupled climate models. *J. Climate*, **19**, 4605–4630, https://doi.org/10.1175/JCLI3884.1.

——, F. Giorgi, and K. E. Trenberth, 1999a: Observed and model-simulated diurnal cycles of precipitation over the contiguous United States. *J. Geophys. Res.*, **104**, 6377–6402, https://doi.org/10.1029/98JD02720.

——, K. E. Trenberth, and T. R. Karl, 1999b: Effects of clouds, soil moisture, precipitation, and water vapor on diurnal temperature range. *J. Climate*, **12**, 2451–2473, https://doi.org/10.1175/1520-0442(1999)012<2451:EOCSMP>2.0.CO;2.

——, X. Lin, and K.-L. Hsu, 2007: The frequency, intensity, and diurnal cycle of precipitation in surface and satellite observations over low- and mid-latitudes. *Climate Dyn.*, **29**, 727–744, https://doi.org/10.1007/s00382-007-0260-y.

Davies, L., R. S. Plant, and S. H. Derbyshire, 2009: A simple model of convection with memory. *J. Geophys. Res.*, **114**, D17202, https://doi.org/10.1029/2008JD011653.

Dirmeyer, P. A., and Coauthors, 2012: Simulating the diurnal cycle of rainfall in global climate models: Resolution versus parameterization. *Climate Dyn.*, **39**, 399–418, https://doi.org/10.1007/s00382-011-1127-9.

Dix, M., and Coauthors, 2019: CSIRO-ARCCSS ACCESS-CM2 model output prepared for CMIP6 CMIP AMIP. Earth System Grid Federation, accessed 17 June 2020, https://doi.org/10.22033/ESGF/CMIP6.4239.

Dufresne, J. L., and Coauthors, 2013: Climate change projections using the IPSL-CM5 Earth System Model: From CMIP3 to CMIP5. *Climate Dyn.*, **40**, 2123–2165, https://doi.org/10.1007/s00382-012-1636-1.

Eyring, V., S. Bony, G. A. Meehl, C. A. Senior, B. Stevens, R. J. Stouffer, and K. E. Taylor, 2016: Overview of the Coupled Model Intercomparison Project phase 6 (CMIP6) experimental design and organization. *Geosci. Model Dev.*, **9**, 1937–1958, https://doi.org/10.5194/gmd-9-1937-2016.

Filho, A. J. P., R. E. Carbone, J. D. Tuttle, and H. A. Karam, 2015: Convective rainfall in Amazonia and adjacent tropics. *Atmos. Climate Sci.*, **5**, 137–161, https://doi.org/10.4236/acs.2015.52011.

Fitzjarrald, D. R., R. K. Sakai, O. L. L. Moraes, R. Cosme de Oliveira, O. C. Acevedo, M. J. Czikowsky, and T. Beldini, 2008: Spatial and temporal rainfall variability near the Amazon-Tapajós confluence. *J. Geophys. Res. Biogeosci.*, **113**, G00B11, https://doi.org/10.1029/2007JG000596.

Geerts, B., and Coauthors, 2017: The 2015 Plains Elevated Convection at Night field project. *Bull. Amer. Meteor. Soc.*, **98**, 767–786, https://doi.org/10.1175/BAMS-D-15-00257.1.

Giles, J. A., R. C. Ruscica, and C. G. Menéndez, 2020: The diurnal cycle of precipitation over South America represented by five gridded datasets. *Int. J. Climatol.*, **40**, 668–686, https://doi.org/10.1002/joc.6229.

Golaz, J.-C., and Coauthors, 2019: The DOE E3SM coupled model version 1: Overview and evaluation at standard resolution. *J. Adv. Model. Earth Syst.*, **11**, 2089–2129, https://doi.org/10.1029/2018MS001603.

Gourley, J. J., Y. Hong, Z. L. Flamig, L. Li, and J. Wang, 2010: Intercomparison of rainfall estimates from radar, satellite, gauge, and combinations for a season of record rainfall. *J. Appl. Meteor. Climatol.*, **49**, 437–452, https://doi.org/10.1175/2009JAMC2302.1.

Greco, S., and Coauthors, 1990: Rainfall and surface kinematic conditions over central Amazonia during ABLE 2B. *J. Geophys. Res.*, **95**, 17 001–17 014, https://doi.org/10.1029/JD095iD10p17001.

Guichard, F., and Coauthors, 2004: Modelling the diurnal cycle of deep precipitating convection over land with cloud-resolving models and single-column models. *Quart. J. Roy. Meteor. Soc.*, **130**, 3139–3172, https://doi.org/10.1256/qj.03.145.

Hazeleger, W., C. Severijns, T. Semmler, S. Stefanescu, and S. Yang, 2010: EC-Earth: A seamless Earth-system prediction approach in action. *Bull. Amer. Meteor. Soc.*, **91**, 1357–1364, https://doi.org/10.1175/2010BAMS2877.1.

Held, I. M., and Coauthors, 2019: Structure and performance of GFDL's CM4.0 climate model. *J. Adv. Model. Earth Syst.*, **11**, 3691–3727, https://doi.org/10.1029/2019MS001829.

Hodges, K. I., and C. D. Thorncroft, 1997: Distribution and statistics of African mesoscale convective weather systems based on the ISCCP Meteosat imagery. *Mon. Wea. Rev.*, **125**, 2821–2837, https://doi.org/10.1175/1520-0493(1997)125<2821:DASOAM>2.0.CO;2.

Hourdin, F., and Coauthors, 2020: LMDZ6A: The atmospheric component of the IPSL climate model with improved and better tuned physics. *J. Adv. Model. Earth Syst.*, **12**, e2019MS001892, https://doi.org/10.1029/2019MS001892.

Houze, R. A., 2014: Clouds and precipitation associated with hills and mountains. *International Geophysics*, R. A. Houze, Ed., Academic Press, 369–402.

Huffman, G. J., and Coauthors, 2007: The TRMM multisatellite precipitation analysis (TMPA): Quasi-global, multiyear, combined-sensor precipitation estimates at fine scales. *J. Hydrometeor.*, **8**, 38–55, https://doi.org/10.1175/JHM560.1.

——, D. T. Bolvin, D. Braithwaite, K. Hsu, R. Joyce, and P. Xie, 2019: Algorithm Theoretical Basis Document (ATBD) version 5.2 for the NASA Global Precipitation Measurement (GPM) Integrated Multi-satellite Retrievals for GPM (I-MERG). NASA GPM, 38 pp., https://gpm.nasa.gov/sites/default/files/document_files/IMERG_ATBD_V5.2_0.pdf.

Janowiak, J. E., V. E. Kousky, and R. J. Joyce, 2005: Diurnal cycle of precipitation determined from the CMORPH high spatial and temporal resolution global precipitation analyses. *J. Geophys. Res. Atmos.*, **110**, D23105, https://doi.org/10.1029/2005JD006156.

Ji, D., and Coauthors, 2014: Description and basic evaluation of Beijing Normal University Earth System Model (BNU-ESM) version 1. *Geosci. Model Dev.*, **7**, 2039–2064, https://doi.org/10.5194/gmd-7-2039-2014.

Jiang, X., N.-C. Lau, and S. A. Klein, 2006: Role of eastward propagating convection systems in the diurnal cycle and seasonal

mean of summertime rainfall over the U.S. Great Plains. *Geophys. Res. Lett.*, **33**, L19809, https://doi.org/10.1029/2006GL027022.

Joyce, R. J., J. E. Janowiak, P. A. Arkin, and P. Xie, 2004: CMORPH: A method that produces global precipitation estimates from passive microwave and infrared data at high spatial and temporal resolution. *J. Hydrometeor.*, **5**, 487–503, https://doi.org/10.1175/1525-7541(2004)005<0487:CAMTPG>2.0.CO;2.

Junquas, C., K. Takahashi, T. Condom, J.-C. Espinoza, S. Chavez, J.-E. Sicart, and T. Lebel, 2018: Understanding the influence of orography on the precipitation diurnal cycle and the associated atmospheric processes in the central Andes. *Climate Dyn.*, **50**, 3995–4017, https://doi.org/10.1007/s00382-017-3858-8.

Kalman, R. E., 1960: A new approach to linear filtering and prediction problems. *J. Basic Eng.*, **82**, 35–45, https://doi.org/10.1115/1.3662552.

Kikuchi, K., and B. Wang, 2008: Diurnal precipitation regimes in the global tropics. *J. Climate*, **21**, 2680–2696, https://doi.org/10.1175/2007JCLI2051.1.

Lee, M.-I., and Coauthors, 2007a: Sensitivity to horizontal resolution in the AGCM simulations of warm season diurnal cycle of precipitation over the United States and northern Mexico. *J. Climate*, **20**, 1862–1881, https://doi.org/10.1175/JCLI4090.1.

——, and Coauthors, 2007b: An analysis of the warm-season diurnal cycle over the continental United States and northern Mexico in general circulation models. *J. Hydrometeor.*, **8**, 344–366, https://doi.org/10.1175/JHM581.1.

——, S. D. Schubert, M. J. Suarez, J.-K. E. Schemm, H.-L. Pan, J. Han, and S.-H. Yoo, 2008: Role of convection triggers in the simulation of the diurnal cycle of precipitation over the United States Great Plains in a general circulation model. *J. Geophys. Res.*, **113**, D02111, https://doi.org/10.1029/2007JD008984.

Lee, W. L., and Coauthors, 2020: Taiwan Earth System Model version 1: Description and evaluation of mean state. *Geosci. Model Dev.*, **13**, 3887–3904, https://doi.org/10.5194/gmd-13-3887-2020.

Li, L., and Coauthors, 2013: The Flexible Global Ocean-Atmosphere-Land System Model, Grid-point version 2: FGOALS-g2. *Adv. Atmos. Sci.*, **30**, 543–560, https://doi.org/10.1007/s00376-012-2140-6.

——, and Coauthors, 2020: The Flexible Global Ocean-Atmosphere-Land System Model Grid-point version 3 (FGOALS-g3): Description and evaluation. *J. Adv. Model. Earth Syst.*, **12**, e2019MS002012, https://doi.org/10.1029/2019MS002012.

Liang, X.-Z., L. Li, A. Dai, and K. E. Kunkel, 2004: Regional climate model simulation of summer precipitation diurnal cycle over the United States. *Geophys. Res. Lett.*, **31**, L24208, https://doi.org/10.1029/2004GL021054.

Liu, X., A. Bai, and C. Liu, 2009: Diurnal variations of summertime precipitation over the Tibetan Plateau in relation to orographically-induced regional circulations. *Environ. Res. Lett.*, **4**, 045203, https://doi.org/10.1088/1748-9326/4/4/045203.

Machado, L. A. T., H. Laurent, N. Dessay, and I. Miranda, 2004: Seasonal and diurnal variability of convection over the Amazonia: A comparison of different vegetation types and large scale forcing. *Theor. Appl. Climatol.*, **78**, 61–77, https://doi.org/10.1007/s00704-004-0044-9.

Mapes, B., and R. Neale, 2011: Parameterizing convective organization to escape the entrainment dilemma. *J. Adv. Model. Earth Syst.*, **3**, M06004, https://doi.org/10.1029/2011MS000042.

Marsham, J. H., S. B. Trier, T. M. Weckwerth, and J. W. Wilson, 2011: Observations of elevated convection initiation leading to a surface-based squall line during 13 June IHOP_2002. *Mon. Wea. Rev.*, **139**, 247–271, https://doi.org/10.1175/2010MWR3422.1.

Massonnet, F., M. Ménégoz, M. Acosta, X. Yepes-Arbós, E. Exarchou, and F. J. Doblas-Reyes, 2020: Replicability of the EC-Earth3 Earth system model under a change in computing environment. *Geosci. Model Dev.*, **13**, 1165–1178, https://doi.org/10.5194/gmd-13-1165-2020.

Mauritsen, T., and Coauthors, 2019: Developments in the MPI-M Earth System Model version 1.2 (MPI-ESM1.2) and its response to increasing CO_2. *J. Adv. Model. Earth Syst.*, **11**, 998–1038, https://doi.org/10.1029/2018MS001400.

Mori, S., and Coauthors, 2004: Diurnal land–sea rainfall peak migration over Sumatera Island, Indonesian Maritime Continent, observed by TRMM satellite and intensive rawinsonde soundings. *Mon. Wea. Rev.*, **132**, 2021–2039, https://doi.org/10.1175/1520-0493(2004)132<2021:DLRPMO>2.0.CO;2.

Neale, R. B., and Coauthors, 2010: Description of the NCAR Community Atmosphere Model (CAM 4.0). NCAR Tech. Note NCAR/TN-485+STR, 212 pp., www.cesm.ucar.edu/models/ccsm4.0/cam/docs/description/cam4_desc.pdf.

Nesbitt, S. W., D. J. Gochis, and T. J. Lang, 2008: The diurnal cycle of clouds and precipitation along the Sierra Madre Occidental observed during NAME-2004: Implications for warm season precipitation estimation in complex terrain. *J. Hydrometeor.*, **9**, 728–743, https://doi.org/10.1175/2008JHM939.1.

Nyquist, H., 1928: Certain topics in telegraph transmission theory. *Trans. Amer. Inst. Electr. Eng.*, **47**, 617–644, https://doi.org/10.1109/T-AIEE.1928.5055024.

Pan, D.-M., and D. D. A. Randall, 1998: A cumulus parameterization with a prognostic closure. *Quart. J. Roy. Meteor. Soc.*, **124**, 949–981, https://doi.org/10.1002/qj.49712454714.

Park, S., 2014a: A unified convection scheme (UNICON). Part I: Formulation. *J. Atmos. Sci.*, **71**, 3902–3930, https://doi.org/10.1175/JAS-D-13-0233.1.

——, 2014b: A unified convection scheme (UNICON). Part II: Simulation. *J. Atmos. Sci.*, **71**, 3931–3973, https://doi.org/10.1175/JAS-D-13-0234.1.

——, J. Shin, S. Kim, E. Oh, and Y. Kim, 2019: Global climate simulated by the Seoul National University Atmosphere Model version 0 with a Unified Convection Scheme (SAM0-UNICON). *J. Climate*, **32**, 2917–2949, https://doi.org/10.1175/JCLI-D-18-0796.1.

Pendergrass, A. G., P. J. Gleckler, L. R. Leung, and C. Jakob, 2020: Benchmarking simulated precipitation in Earth system models. *Bull. Amer. Meteor. Soc.*, **101**, E814–E816, https://doi.org/10.1175/BAMS-D-19-0318.1.

Rasch, P. J., and Coauthors, 2019: An overview of the atmospheric component of the Energy Exascale Earth System Model. *J. Adv. Model. Earth Syst.*, **11**, 2377–2411, https://doi.org/10.1029/2019MS001629.

Rio, C., F. Hourdin, J. Y. Grandpeix, and J. P. Lafore, 2009: Shifting the diurnal cycle of parameterized deep convection over land. *Geophys. Res. Lett.*, **36**, L07809, https://doi.org/10.1029/2008GL036779.

Rowell, D. P., and J. R. Milford, 1993: On the generation of African squall lines. *J. Climate*, **6**, 1181–1193, https://doi.org/10.1175/1520-0442(1993)006<1181:OTGOAS>2.0.CO;2.

Santos e Silva, C. M., R. Gielow, and S. R. de Freitas, 2009: Diurnal and semidiurnal rainfall cycles during the rain season in SW Amazonia, observed via rain gauges and estimated using S-band radar. *Atmos. Sci. Lett.*, **10**, 87–93, https://doi.org/10.1002/asl.214.

Sato, T., 2013: Mechanism of orographic precipitation around the Meghalaya Plateau associated with intraseasonal oscillation and the diurnal cycle. *Mon. Wea. Rev.*, **141**, 2451–2466, https://doi.org/10.1175/MWR-D-12-00321.1.

——, H. Miura, M. Satoh, Y. N. Takayabu, and Y. Wang, 2009: Diurnal cycle of precipitation in the tropics simulated in a

global cloud-resolving model. *J. Climate*, **22**, 4809–4826, https://doi.org/10.1175/2009JCLI2890.1.

Scoccimarro, E., and Coauthors, 2011: Effects of tropical cyclones on ocean heat transport in a high-resolution coupled general circulation model. *J. Climate*, **24**, 4368–4384, https://doi.org/10.1175/2011JCLI4104.1.

Serra, Y. L., and M. J. McPhaden, 2003: Multiple time- and space-scale comparisons of ATLAS buoy rain gauge measurements with TRMM satellite precipitation measurements. *J. Appl. Meteor.*, **42**, 1045–1059, https://doi.org/10.1175/1520-0450(2003)042<1045:MTASCO>2.0.CO;2.

Shannon, C. E., 1949: Communication in the presence of noise. *Proc. IRE*, **37**, 10–21, https://doi.org/10.1109/JRPROC.1949.232969.

Sorooshian, S., K.-L. Hsu, X. Gao, H. V. Gupta, B. Imam, and D. Braithwaite, 2000: Evaluation of PERSIANN system satellite-based estimates of tropical rainfall. *Bull. Amer. Meteor. Soc.*, **81**, 2035–2046, https://doi.org/10.1175/1520-0477(2000)081<2035:EOPSSE>2.3.CO;2.

——, X. Gao, K. Hsu, R. A. Maddox, Y. Hong, H. V. Gupta, and B. Imam, 2002: Diurnal variability of tropical rainfall retrieved from combined GOES and TRMM satellite information. *J. Climate*, **15**, 983–1001, https://doi.org/10.1175/1520-0442(2002)015<0983:DVOTRR>2.0.CO;2.

Sun, Q., C. Miao, Q. Duan, H. Ashouri, S. Sorooshian, and K. L. Hsu, 2018: A review of global precipitation data sets: Data sources, estimation, and intercomparisons. *Rev. Geophys.*, **56**, 79–107, https://doi.org/10.1002/2017RG000574.

Tanaka, L. M. S., P. Satyamurty, and L. A. T. Machado, 2014: Diurnal variation of precipitation in central Amazon basin. *Int. J. Climatol.*, **34**, 3574–3584, https://doi.org/10.1002/joc.3929.

Tang, S., and Coauthors, 2016: Large-scale vertical velocity, diabatic heating and drying profiles associated with seasonal and diurnal variations of convective systems observed in the GoAmazon2014/5 experiment. *Atmos. Chem. Phys.*, **16**, 14 249–14 264, https://doi.org/10.5194/acp-16-14249-2016.

——, and Coauthors, 2019: Differences in eddy-correlation and energy-balance surface turbulent heat flux measurements and their impacts on the large-scale forcing fields at the ARM SGP site. *J. Geophys. Res. Atmos.*, **124**, 3301–3318, https://doi.org/10.1029/2018JD029689.

Tatebe, H., and Coauthors, 2019: Description and basic evaluation of simulated mean state, internal variability, and climate sensitivity in MIROC6. *Geosci. Model Dev.*, **12**, 2727–2765, https://doi.org/10.5194/gmd-12-2727-2019.

Taylor, K. E., 2001: Summarizing multiple aspects of model performance in a single diagram. *J. Geophys. Res.*, **106**, 7183–7192, https://doi.org/10.1029/2000JD900719.

——, R. J. Stouffer, and G. A. Meehl, 2012: An overview of CMIP5 and the experiment design. *Bull. Amer. Meteor. Soc.*, **93**, 485–498, https://doi.org/10.1175/BAMS-D-11-00094.1.

Tian, B., I. M. Held, N.-C. Lau, and B. J. Soden, 2005: Diurnal cycle of summertime deep convection over North America: A satellite perspective. *J. Geophys. Res.*, **110**, D08108, https://doi.org/10.1029/2004JD005275.

Trenberth, K. E., A. Dai, R. M. Rasmussen, and D. B. Parsons, 2003: The changing character of precipitation. *Bull. Amer. Meteor. Soc.*, **84**, 1205–1218, https://doi.org/10.1175/BAMS-84-9-1205.

——, Y. Zhang, and M. Gehne, 2017: Intermittency in precipitation: Duration, frequency, intensity, and amounts using hourly data. *J. Hydrometeor.*, **18**, 1393–1412, https://doi.org/10.1175/JHM-D-16-0263.1.

Villarini, G., and W. F. Krajewski, 2010: Review of the different sources of uncertainty in single polarization radar-based estimates of rainfall. *Surv. Geophys.*, **31**, 107–129, https://doi.org/10.1007/s10712-009-9079-x.

Voldoire, A., and Coauthors, 2019: Evaluation of CMIP6 DECK experiments with CNRM-CM6-1. *J. Adv. Model. Earth Syst.*, **11**, 2177–2213, https://doi.org/10.1029/2019MS001683.

Volodin, E. M., N. A. Dianskii, and A. V. Gusev, 2010: Simulating present-day climate with the INMCM4.0 coupled model of the atmospheric and oceanic general circulations. *Izv. Atmos. Ocean. Phys.*, **46**, 414–431, https://doi.org/10.1134/S000143381004002X.

Waliser, D., and Coauthors, 2020: Observations for Model Intercomparison Project (Obs4MIPs): Status for CMIP6. *Geosci. Model Dev.*, **13**, 2945–2958, https://doi.org/10.5194/gmd-13-2945-2020.

Walters, D., and Coauthors, 2019: The Met Office Unified Model Global Atmosphere 7.0/7.1 and JULES Global Land 7.0 configurations. *Geosci. Model Dev.*, **12**, 1909–1963, https://doi.org/10.5194/gmd-12-1909-2019.

Wang, Y.-C., H.-L. Pan, and H.-H. Hsu, 2015: Impacts of the triggering function of cumulus parameterization on warm-season diurnal rainfall cycles at the Atmospheric Radiation Measurement Southern Great Plains site. *J. Geophys. Res. Atmos.*, **120**, 10 681–610 702, https://doi.org/10.1002/2015JD023337.

——, S. Xie, S. Tang, and W. Lin, 2020: Evaluation of an improved convective triggering function: Observational evidence and SCM tests. *J. Geophys. Res. Atmos.*, **125**, e2019JD031651, https://doi.org/10.1029/2019JD031651.

Watanabe, M., and Coauthors, 2010: Improved climate simulation by MIROC5: Mean states, variability, and climate sensitivity. *J. Climate*, **23**, 6312–6335, https://doi.org/10.1175/2010JCLI3679.1.

Williams, D. N., and Coauthors, 2016: A global repository for planet-sized experiments and observations. *Bull. Amer. Meteor. Soc.*, **97**, 803–816, https://doi.org/10.1175/BAMS-D-15-00132.1.

Worku, L. Y., A. Mekonnen, and C. J. Schreck III, 2019: Diurnal cycle of rainfall and convection over the Maritime Continent using TRMM and ISCCP. *Int. J. Climatol.*, **39**, 5191–5200, https://doi.org/10.1002/joc.6121.

Wu, T., 2012: A mass-flux cumulus parameterization scheme for large-scale models: Description and test with observations. *Climate Dyn.*, **38**, 725–744, https://doi.org/10.1007/s00382-011-0995-3.

——, and Coauthors, 2014: An overview of BCC Climate System Model development and application for climate change studies. *J. Meteor. Res.*, **28**, 34–56, https://doi.org/10.1007/s13351-014-3041-7.

——, and Coauthors, 2019: The Beijing Climate Center Climate System Model (BCC_CSM): The main progress from CMIP5 to CMIP6. *Geosci. Model Dev.*, **12**, 1573–1600, https://doi.org/10.5194/gmd-12-1573-2019.

Xie, P., and P. A. Arkin, 1997: Global precipitation: A 17-year monthly analysis based on gauge observations, satellite estimates, and numerical model outputs. *Bull. Amer. Meteor. Soc.*, **78**, 2539–2558, https://doi.org/10.1175/1520-0477(1997)078<2539:GPAYMA>2.0.CO;2.

——, R. Joyce, S. Wu, S.-H. Yoo, Y. Yarosh, F. Sun, and R. Lin, 2017: Reprocessed, bias-corrected CMORPH global high-resolution precipitation estimates from 1998. *J. Hydrometeor.*, **18**, 1617–1641, https://doi.org/10.1175/JHM-D-16-0168.1.

Xie, S., and Coauthors, 2002: Intercomparison and evaluation of cumulus parametrizations under summertime midlatitude continental conditions. *Quart. J. Roy. Meteor. Soc.*, **128**, 1095–1135, https://doi.org/10.1256/003590002320373229.

——, R. T. Cederwall, and M. Zhang, 2004: Developing long-term single-column model/cloud system–resolving model forcing data using numerical weather prediction products constrained by surface and top of the atmosphere observations. *J. Geophys. Res.*, **109**, D01104, https://doi.org/10.1029/2003JD004045.

——, and Coauthors, 2010: Clouds and more: ARM climate modeling best estimate data. *Bull. Amer. Meteor. Soc.*, **91**, 13–20, https://doi.org/10.1175/2009BAMS2891.1.

——, Y. Zhang, S. E. Giangrande, M. P. Jensen, R. McCoy, and M. Zhang, 2014: Interactions between cumulus convection and its environment as revealed by the MC3E sounding array. *J. Geophys. Res. Atmos.*, **119**, 11 784–11 808, https://doi.org/10.1002/2014JD022011.

——, and Coauthors, 2018: Understanding cloud and convective characteristics in version 1 of the E3SM atmosphere model. *J. Adv. Model. Earth Syst.*, **10**, 2618–2644, https://doi.org/10.1029/2018MS001350.

——, and Coauthors, 2019: Improved diurnal cycle of precipitation in E3SM with a revised convective triggering function. *J. Adv. Model. Earth Syst.*, **11**, 2290–2310, https://doi.org/10.1029/2019MS001702.

Yang, B., M. Wang, G. J. Zhang, Z. Guo, Y. Qian, A. Huang, and Y. Zhang, 2020: Simulated precipitation diurnal variation with a deep convective closure subject to shallow convection in Community Atmosphere Model version 5 coupled with CLUBB. *J. Adv. Model. Earth Syst.*, **12**, e2020MS002050, https://doi.org/10.1029/2020MS002050.

Yang, G.-Y., and J. Slingo, 2001: The diurnal cycle in the tropics. *Mon. Wea. Rev.*, **129**, 784–801, https://doi.org/10.1175/1520-0493(2001)129<0784:TDCITT>2.0.CO;2.

Yukimoto, S., and Coauthors, 2019: The Meteorological Research Institute Earth System Model version 2.0, MRI-ESM2.0: Description and basic evaluation of the physical component. *J. Meteor. Soc. Japan*, **97**, 931–965, https://doi.org/10.2151/jmsj.2019-051.

Zhang, M., and J. Lin, 1997: Constrained variational analysis of sounding data based on column-integrated budgets of mass, heat, moisture, and momentum: Approach and application to ARM measurements. *J. Atmos. Sci.*, **54**, 1503–1524, https://doi.org/10.1175/1520-0469(1997)054<1503:CVAOSD>2.0.CO;2.

——, S. Xie, R. T. Cederwall, and J. J. Yio, 2001: Description of the ARM operational objective analysis system. ARM Tech. Rep. ARM-TR-005, 26 pp.

Zhao, M., I. M. Held, S.-J. Lin, and G. A. Vecchi, 2009: Simulations of global hurricane climatology, interannual variability, and response to global warming using a 50-km resolution GCM. *J. Climate*, **22**, 6653–6678, https://doi.org/10.1175/2009JCLI3049.1.

Zhao, T., and A. Yatagai, 2014: Evaluation of TRMM 3B42 product using a new gauge-based analysis of daily precipitation over China. *Int. J. Climatol.*, **34**, 2749–2762, https://doi.org/10.1002/joc.3872.

Zheng, X., J. C. Golaz, S. Xie, Q. Tang, W. Lin, M. Zhang, H. Y. Ma, and E. L. Roesler, 2019: The summertime precipitation bias in E3SM atmosphere model version 1 over the central United States. *J. Geophys. Res. Atmos.*, **124**, 8935–8952, https://doi.org/10.1029/2019JD030662.

Zhou, T., R. Yu, H. Chen, A. Dai, and Y. Pan, 2008: Summer precipitation frequency, intensity, and diurnal cycle over China: A comparison of satellite data with rain gauge observations. *J. Climate*, **21**, 3997–4010, https://doi.org/10.1175/2008JCLI2028.1.